Fines-Induced Shear Band Thickening in Gap-Graded Soils: Evidence from Digital Image and Volume Correlations

Shijin Li[1], Alexandre Sac-Morane[2], Jeroen Soete[3], Hannes Claes[4], Johan Vanhulst[5], Hadrien Rattez[6]

[1] Institute of Mechanics, Materials and Civil Engineering, Université Catholique de Louvain, Louvain-la-Neuve, 1348, Belgium. shijin.li@uclouvain.be. https://orcid.org/0000-0002-2918-3934.

[2] Institute of Mechanics, Materials and Civil Engineering, Université Catholique de Louvain, Louvain-la-Neuve, 1348, Belgium. alexandre.sac-morane@enpc.fr. https://orcid.org/0009-0008-5454-8107.

[3] Department of Materials Engineering, Katholieke Universiteit Leuven, Belgium. jeroen.soete@kuleuven.be. https://orcid.org/0000-0003-3357-4070.

[4] Department of Earth and Environmental Sciences, KU Leuven University, Celestijnenlaan 200E, 3001 Heverlee, Belgium. hannes.claes1@kuleuven.be. https://orcid.org/0000-0002-2424-6975.

[5] Department of Materials Engineering, Katholieke Universiteit Leuven, Belgium. johan.vanhulst@kuleuven.be.

[6] Institute of Mechanics, Materials and Civil Engineering, Université Catholique de Louvain, Louvain-la-Neuve, 1348, Belgium. hadrien.rattez@uclouvain.be. https://orcid.org/0000-0002-7245-6563.

* (Corresponding author) Email: hadrien.rattez@uclouvain.be

Figures: 21 (please refer to figure files for higher quality versions)

Tables: 2

Main text word count: 7902

ABSTRACT

Shear band thickness is a critical parameter governing strain localisation and post-peak strength degradation in granular soils. However, its relationship with fines content and the consistency between surface- and volume-based measurement techniques remain insufficiently understood. This study investigates the evolution and residual thickness of shear bands in gap-graded sands with fines contents ranging from 0% to 40%, using triaxial tests equipped with either digital image correlation (DIC) or digital volume correlation (DVC). The stress-strain response and friction angle variations with varying mean particle size and fines content align well with, and further validate, previous experimental and numerical studies. DIC measurements, derived from surface strain fields, are compared with DVC measurements obtained from internal deformation fields reconstructed via X-ray computed tomography. Results show that increasing fines content promotes both the development and thickening of shear bands, with trends consistently captured by both techniques. Shear bands became clearly identifiable at axial strains of 5.0-5.8%, coinciding with the end of strain softening and transition to residual strength. DVC revealed early, non-uniform internal strain localisation and secondary shear plane formation, features not captured by DIC. The residual shear band thickness normalised with mean particle size increased linearly with fines content from ~7.6 to ~11.7, showing that the shear band of sand is not only controlled by the mean particle size but also from fines content. These findings provide new insights into the role of fines in strain localisation, guide the selection of experimental methods for shear band characterisation, and offer valuable data for calibrating and validating numerical models of soil failure mechanisms.

Keywords: gap-graded soil; strain localisation; shear band thickness; digital image correlation; digital volume correlation

1. Introduction

Strain localisation in soils, often manifested as shear bands, is a critical phenomenon governing the failure and post-peak response of geomaterials [17, 19, 45, 59, 64]. Accurate characterisation of shear band size is essential for linking microscale particle movements with macroscale failure [24, 60], validating constitutive and numerical models [21, 22, 42], and improving the design and safety of geotechnical structures [13, 43, 50].

The thickness of shear bands, as reported from experimental observations in the literature, typically falls within 8–20 times the mean particle size [4, 19, 24, 35, 41], which is a key parameter governing strain localisation and post-peak strength degradation in granular soils. Quantitative characterisation of this localisation process has been pursued through a wide array of imaging-based experimental approaches. These include surface-based techniques such as photogrammetry [19], strain markers [54], and digital image correlation (DIC) applied to external sample surfaces [5, 12, 41, 44, 46] and photoelastic particle imaging coupled with DIC [24]. In contrast, volumetric methods, such as X-ray computed tomography (X-ray CT) combined with digital volume correlation (DVC) [6, 18, 25, 28, 40, 51, 65], void ratio mapping [4], and photoelastic particle imaging coupled with DVC [38], characterise internal deformation by resolving the specimen's internal structure, enabling detailed analysis of the strain localisation process within the volume of interest. Together, these experimental approaches offer complementary insight into the structure and kinematics of strain localisation. Among them, DIC and DVC are particularly well-suited for tracking the full evolution of deformation from the onset of shearing to the residual state, respectively at the surface or within the specimen's bulk volume. While DIC has been applied for estimating shear band thickness from surface strain fields, DVC has predominantly been used to investigate internal microstructural changes and only few studies explicitly quantified shear band thickness. With recent advances in high-resolution DVC and computing technologies, alongside the growing demand for detailed internal strain measurements, a comparative assessment of DIC and DVC is essential to elucidate their respective strengths, limitations, and roles in future shear band characterisation.

In addition, most experimental investigations of strain localisation in sands have focused on granular materials with a narrow particle size distribution (PSD), typically characterised by a maximum-to-minimum particle size ratio below 10 [4, 5, 24, 40, 65] or by a uniformity coefficient of particle size distribution close to 1 [18, 46]. However, the influence of the fines content (FC), which is increasingly recognised as a key factor affecting the fundamental mechanical behaviour of sands [30, 33, 36, 52], has received comparatively less experimental attention in the context of strain localisation. A few studies have explored the effect of broader particle size distributions and observed that well-graded sands tend to develop thicker shear bands than uniform sands [46, 41]. Nevertheless, the specific role of fines in shear band formation and evolution remains unclear, and no systematic or quantitative comparison has yet been conducted to examine how shear band thickness varies with increasing fines content.

Despite its recognised influence on the mechanical behaviour of sands, the role of the fines content in shear band development has not been comprehensively investigated, and existing applications of DIC to shear band characterisation have largely been limited to capturing surface displacements, without providing direct insight into internal microstructural evolution. This study aims to: (1) compare the methodologies and effectiveness of characterising shear bands using triaxial shearing test with DIC (Triaxial-DIC) and DVC (Triaxial-DVC); (2) investigate the effects of fines content on shear band evolution and residual shear band thickness. Hence, a programme of triaxial shearing tests incorporating either DIC or DVC was performed on sand samples with varying fines content. The development and residual thickness of shear bands were systematically compared between the two methods. The results provide new insights into the role of fines in strain localisation, confirm the consistency between surface- and volume-based measurements of shear band thickness, and highlight the respective advantages of DVC in capturing internal mechanisms. These findings also offer guidance for the design of future experiments, the development of theoretical frameworks, and the validation and interpretation of numerical models concerning soil failure mechanisms and strain localisation behaviour.

2. Material and methods

2.1 Testing material and sample preparation

The testing gap-graded soil was formed by mixing two base materials: the coarser fraction of North Sea Sand (NSS) and the finer fraction consisting of Silica Gel 60 (sourced from commercial supplier Merck KGaA, with a particle size range of 10-75 μm). Three sets of samples were prepared for different purposes. The first set (Tests No. 1-3 in Table 1) comprised three uniform fractions of NSS with particle size ranges of 180-300 μm (denoted as NSS1), 300-425 μm (denoted as NSS2), and 425-600 μm (denoted as NSS3), obtained by dry sieving from a batch of original NSS. The PSDs of the Silica Gel 60, NSS1, NSS2 and NSS3 are shown in Fig. 1(a). The second set comprised 300-425 μm NSS mixed with varying fines content yet maintained a similar d_{50}. NSS with similar d_{50} but fines content ranges from 10%-40% refer to conditions where finer soils either loosely occupy the voids between coarser sand grains, contributing negligibly to stress transfer during shearing (termed as 'underfilled', typically for a FC less than ~25%), or completely fill the voids and actively participate in stress transfer (termed 'overfilled', for FC greater than ~35%) [53, 57]. A 'transitional' soil condition is recognized when the FC falls within the 25-35% range, representing a shift in stress transfer behaviour between coarse- and fines-dominated stress transfer regimes. The third set consists of NSS with different d_{50} but same fine content (20%). The PSDs of these soils are shown in Fig. 1 and a summary of the testing materials and conditions is given in Table 1. To isolate the influence of fines content, all tests were conducted under consistent conditions, including standard triaxial load path, identical confining pressure, relative density, and sample slenderness, which are known to govern shear band thickness [19, 23, 24].

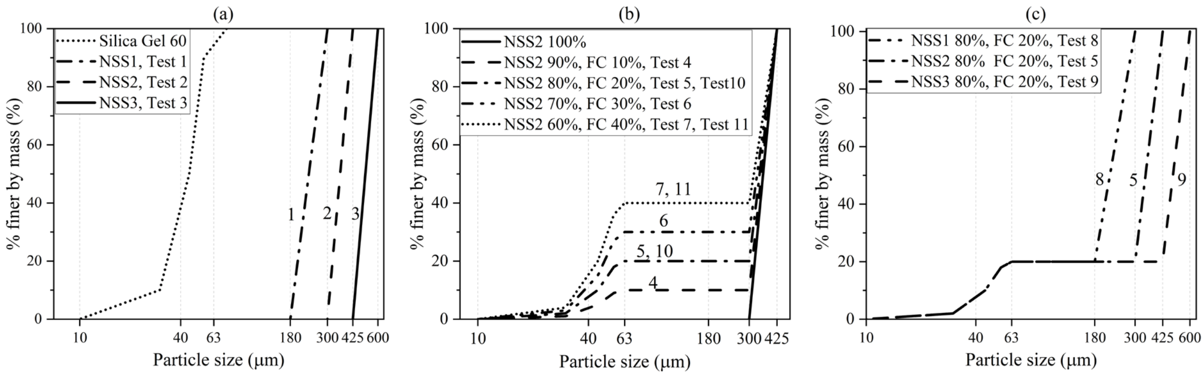

Fig. 1. Particle size distribution of the testing soils: (a) Silica Gel 60, NSS1, NSS2, and NSS3; (b) NSS2 with varying fines content; (c) NSS1, NSS2, and NSS3 each with 20% of fines content

Selected shape descriptors, including aspect ratio, roundness, circularity, and solidity, were analysed using Fiji ImageJ software on reconstructed 2D cross-sections of NSS particles obtained through X-ray CT scanning. An ellipse of best fit was used to determine each particle's major and minor axes. The shape descriptors were calculated as follows [49]: aspect ratio (major axis/minor axis), roundness (4×area/(π × major axis^2)), circularity (4π/perimeter^2), and solidity (area/convex area). Measurements averaged from 2,478 particles yielded the following values: aspect ratio 16.7, roundness 0.65, circularity 0.74, and solidity 0.83.

The relative density, $D_r = (e_{max} - e)/(e_{max} - e_{min})$, was selected as the parameter to quantify the density of the sand-fines mixture because: (a) the global maximum and minimum void ratios (e_{max} and e_{min}, respectively) of the sand-fines mixture change with fines content [34, 70]; (b) soil behaviours exhibits only minor dependency on the inter-granular void ratio [14, 58]; and (c) a consistent relative density is more experimentally practical for sample preparation and is commonly used by others. The values of e_{max} and e_{min} were determined following ASTM D4253 [8] and ASTM D4254 [9]. All samples with varying fines content were prepared at a consistent relative density of 70%. Fig. 2 shows the variations of e_{max} and e_{min} as the fines content ranges from 0–40% by mass. These variations exhibit a trend similar to those reported in the literature for different sand-fines mixtures [34, 57, 69, 70].

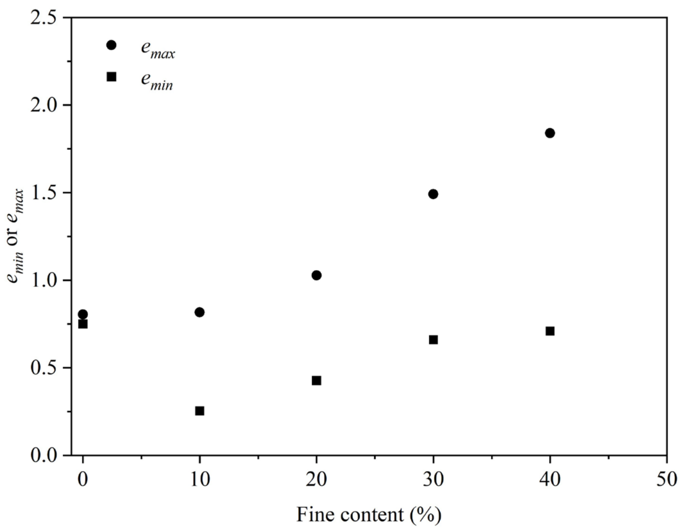

Fig. 2. e_{min} and e_{max} evolutions of NSS2 mixed with varying fines content.

Two sizes of cylindrical samples were prepared using these materials: 38 mm in diameter and 76 mm in height for Triaxial-DIC, and 20 mm in diameter and 40 mm in height for Triaxial-DVC. The largest particle sizes for the 38 mm and 20 mm diameter samples were 0.6 mm and 0.425 mm, respectively. This results in the smallest ratios of sample diameter to largest particle diameter being 63.33 and 47.06, respectively. These ratios are sufficiently large to ensure that the triaxial test results are not significantly affected by particle size [10]. Previous studies have demonstrated that shear band thickness is primarily governed by particle size and remains largely independent of the overall sample size [3]. This finding provides a sound basis for comparing shear band thickness across samples of different sizes.

Samples were prepared by first calculating the required mass of NSS and Silica Gel 60 to achieve the targeted fines content and relative density. These calculated amounts of NSS and silica sand were thoroughly mixed by a combination of shaking for approximately 30 minutes on a high-frequency shaker, followed by manual mixing to ensure homogeneity. The mixture was then deposited layer by layer into a split mould, which was internally lined with a latex membrane and maintained under negative vacuum pressure (-15 kPa). During deposition, a funnel with a long shaft was used to minimize the effects of gravity, thereby reducing the potential for segregation between the two types of sands [34]. After each layer was placed, the technique of 'under-compaction' [31] was applied to gently tamp the sample to the target height, ensuring a relative density (D_r) of about 70%.

Table 1. A summary of testing materials and conditions

Test NO.	Material	Test type	Sample size (mm)	d_{50} (μm)	d_{max} $/d_{min}$	$d_{50\ coarse}$ $/d_{50\ fine}$	Visible shear band?
1	NSS1 (180-300)	Triaxial-DIC	38×76	232	1.67	-	Yes
2	NSS2 (300-425)	Triaxial-DIC	38×76	357	1.42	-	Yes
3	NSS3 (425-600)	Triaxial DIC	38×76	505	1.41	-	No
4	90% NSS2, 10% fines	Triaxial-DIC	38×76	350	42.5	7.98	Yes
5	80% NSS2, 20% fines	Triaxial-DIC	38×76	341	42.5	7.98	Yes
6	70% NSS2, 30% fines	Triaxial-DIC	38×76	331	42.5	7.98	Yes
7	60% NSS2, 40% fines	Triaxial-DIC	38×76	316	42.5	7.98	Yes
8	80% NSS1, 20% fines	Triaxial-DIC	38×76	221	30	5.19	Yes
9	80% NSS3, 20% fines	Triaxial-DIC	38×76	487	60	11.30	Yes
10	80% NSS2, 20% fines	Triaxial-DVC	20×40	341	42.5	7.98	Yes
11	60% NSS2, 40% fines	Triaxial-DVC	20×40	316	42.5	7.98	Yes

Note: d_{xx} denotes the particle size corresponding to xx% by mass for the mixed soil. $d_{50\ coarse}$ and $d_{50\ fine}$

represent the particle size at 50% finer by mass for coarse NSS sand and silica fines, respectively. d_{max} and d_{min} denote the maximum and minimum particle sizes, respectively.

2.2 Triaxial-DIC setup and testing procedures

The Triaxial-DIC setup was broadly similar to that used by Rattez et al. [41]. It consisted of a fixed-ends triaxial loading system with controlled cell pressure, a triaxial data acquisition system, and a DIC image acquisition system (LIMESS Q400 Digital Image Correlation), as shown in Fig. 3 (a) and (b). Standard monotonic shearing tests were conducted on dry samples under a consistent confining pressure of 200 kPa to observe the influence of fines content on shear band thickness using DIC. The initial sample dimensions were 38 mm in diameter and 76 (±0.5) mm in height.

During sample installation, a negative pressure of 10 kPa was applied and maintained to hold the sample in place. A unique and random speckle pattern was applied to the membrane using black spray paint (Fig. 3 (c) and (d)), ensuring consistent pattern visibility between consecutive images and providing distinctive local texture for accurate image analysis. The cell was then filled with de-aired water, and the cell water pressure, controlled by a GDS pressure controller, was gradually increased to 200 kPa at a rate of 10 kPa/min, while keeping the pore pressure open to the atmosphere. A constant axial displacement rate of 0.2 mm/min was applied by moving the pedestal upward, corresponding to an axial strain rate of 4.4×10^{-5} s^{-1}. This axial strain rate, combined with a camera shutter speed of 10 ms, prevented image blurring and allowed a total axial strain of 25% to be achieved within 120 minutes under quasi-static loading conditions.

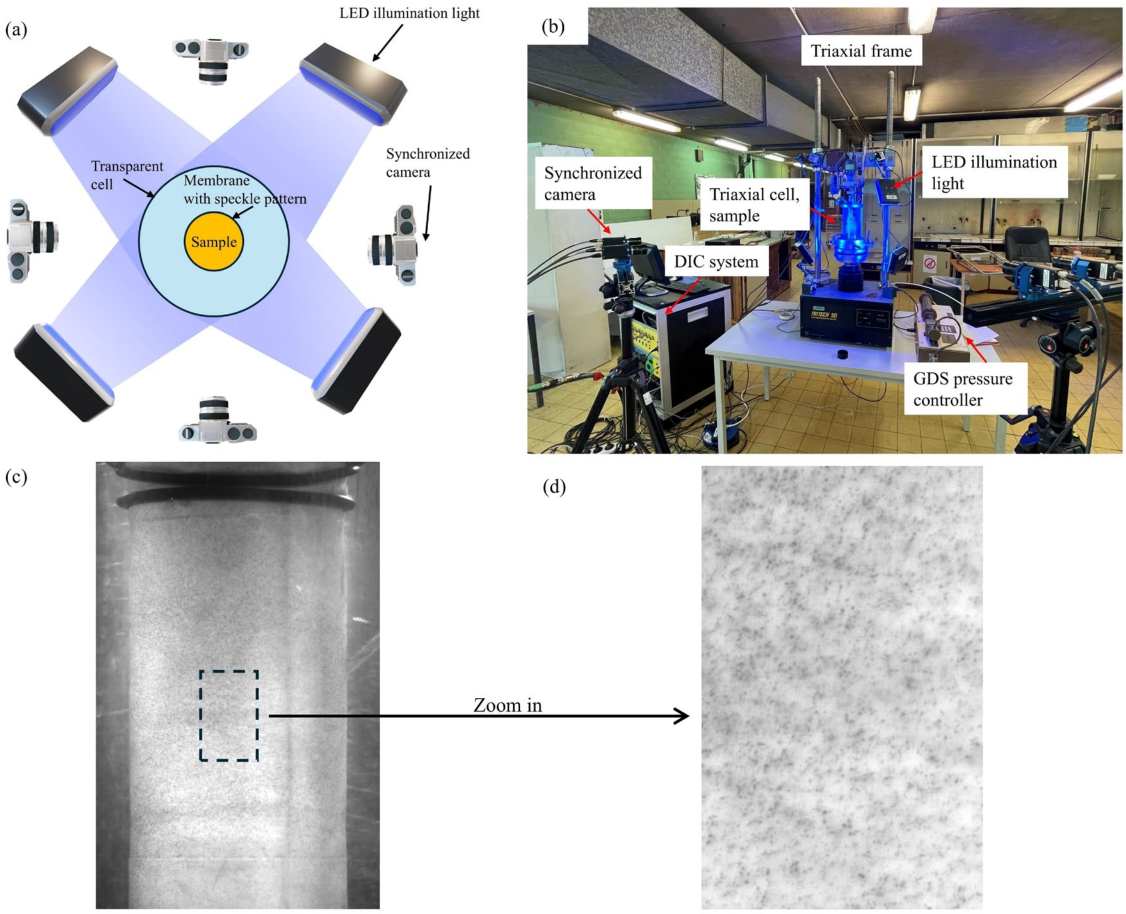

Fig. 3. (a) schematic Triaxial-DIC setup; (b) a photo of Triaxial-DIC setup; (c) a photo of a sample with speckle pattern; (d) close-up view of the speckle pattern.

The Dantec Dynamic Flex DIC hardware (Q-400 DIC system) and software (ISTRA 4D) were used for image acquisition during loading. Four digital cameras were positioned approximately 50 cm from the transparent triaxial cell, with a 90° angle between them, ensuring that at least one camera could capture the initiation and development of the shear band. The ISTRA 4D software allowed the calibration and synchronization of the four cameras in different orientations and spatial positions to evaluate the sample geometry from the captured images. Images were taken every 30 seconds, corresponding to an axial displacement of 0.1 mm (≈0.13% of axial strain) applied to the sample between successive images. A LED illumination system was used during image acquisition to provide flicker-free, medium-intensity light and to minimize potential glare on the transparent cell and speckled membrane. Although lens distortion was negligible after calibration, the cylindrical shape of the sample and refraction at the air-poly methyl methacrylate (PMMA) and PMMA-water interfaces could introduce small magnification effects and variations in apparent distances across the image plane [41], which were corrected during post-processing.

2.3 Triaxial-DVC setup and testing procedures

A compact fixed-ends triaxial and X-ray transparent testing cell (Fig. 4(a)) was developed and integrated with X-ray CT scanning to conduct *in situ* monotonic shearing tests on cylindrical samples measuring 20 mm in diameter and 40 mm in height. The system incorporates an external load cell (Deben CT5000 in-situ testing stage) equipped with a custom-designed pedestal for applying monotonic loads to the sample. This miniaturized triaxial system is mounted on a rotational table positioned between the X-ray source and the detector of a microfocus X-ray CT scanner (TESCAN UniTOM XL) at the KU Leuven XCT Core Facility, as illustrated in Fig. 4 (b) and (c).

The sample was scanned prior to the initiation of shearing at a confining pressure of 200 kPa and subsequently at every 1 mm increment of axial displacement (equivalent to about 2.5% axial strain) until a total displacement of 10 mm was reached, corresponding to a final axial strain of 25%. A constant axial displacement rate of 0.1 mm/min was applied by moving the load cell piston upward, corresponding to an axial strain rate of 4.4×10^{-5} s^{-1}, which is the same as that used in Triaxial-DIC test. After reaching each axial displacement increment, loading was stopped, and a pause of at least 20 minutes was incorporated to ensure sample equilibrium prior to scanning. The scan parameters employed in this study are detailed in Table 2. A voxel edge size of 15 μm is used to image the sample, resulting in 3D tomographic images with dimensions of 1850×1850×2294 voxels. This resolution was sufficient to clearly capture individual NSS particles (d_{50} of NSS2 is 357 μm). The chosen voxel size, similar to that used by Wiebicke et al. [65] for contact detection of sand particles of comparable size, meets the commonly accepted criterion that the voxel size should be at least an order of magnitude smaller than the particle size (i.e., voxel size < d_{50}/20) [39], ensuring adequate resolution to observe and describe the motion of individual particles. However, the silica fines particles in the gap-graded soils, with a d_{50} of 44.7 μm, could not be distinctly identified. Nevertheless, this limitation does not impede the application of DVC techniques using SPAM software [56] for quantitative investigation of gap-graded soils, as demonstrated in previous studies (e.g., Nguyen et al. [37]) and discussed further in Section 3.2.

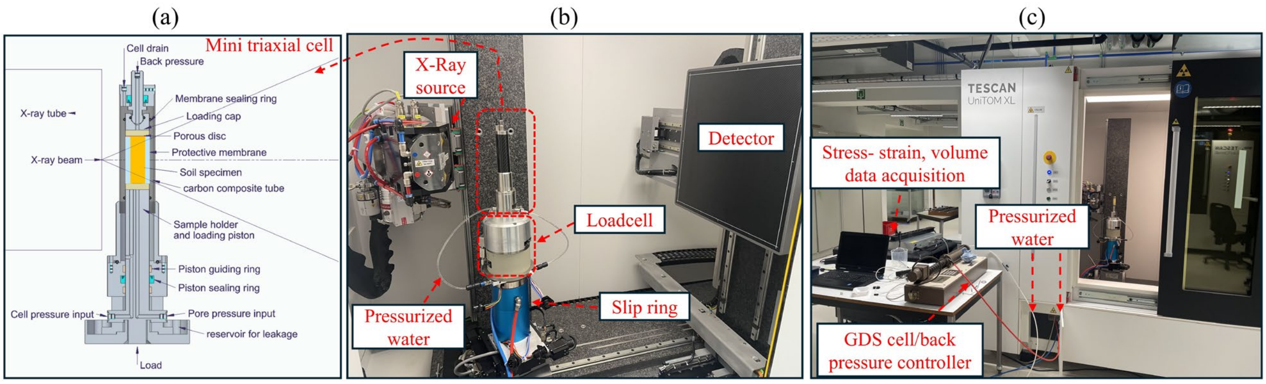

Fig. 4. (a) A sketch of the mini-triaxial cell; (b) The mini- triaxial cell mounted in the X-ray CT scanner; (c) Overview of the test equipment, with external pressure controller and data acquisition system

Table 2 Source, camera and acquisition settings during CT scan

Parameters	Value
Mode	Microfocus
Voltage (kV)	120
Current (μA)	125
Power (W)	15
Exposure time (ms)	180
Time per scan (min)	26
Number of averages	3
Voxel size (μm)	15
Number of projections	2400
Filter	Al, 1 mm

3. DIC and DVC post-processing and shear band thickness calculations

3.1. DIC post-processing and shear band thickness calculations

The numerical correspondence technique by Rattez et al.[41] was employed to track surface deformation between successive images captured from a consistent viewpoint, enabling the extraction of the deformation field and the quantification of shear band thickness. A brief introduction to the DIC method and shear band thickness calculations by Rattez et al. [41] is provided here.

In these tests, although images were captured from four different angles, the image correlation was performed using images from a single camera, ensuring that the clearest view of the shear band to be analysed. A reference length was marked and measured on the filled membrane to determine the pixel size in the images, achieving a photographic resolution of approximately 0.023 mm/pixel. To avoid refraction effects, which may be significant at the sample's edges, and to focus on a region fully contained within the specimen throughout the test, the DIC analysis was restricted to a central window in the images (represented by a square in Fig. 5 (a)). This selection was made independently for each test and typically measured 30 mm in height and 18 mm in width.

This window was subsequently subdivided into a uniform grid of squares, containing 25 and 15 elements in each direction, also shown in Fig. 5 (a). Each square has a side length of 50 pixels, with zero spatial distance between two adjacent squares. This meshing procedure results in the dimensions of the field of displacement being slightly smaller than the selected window, being 28.75 mm in height and 17.25 mm in width. The characteristic patterns within these squares are located in the subsequent image through the application of NCC [27, 32]:

$$\mathrm{NCC}(u,v)=\frac{\sum_{x,y}\mathbf{I}_1(x,y)\mathbf{I}_2(x-u,y-v)}{\sqrt{\sum_{x,y}\mathbf{I}_1(x,y)^2\sum_{x,y}\mathbf{I}_2(x-u,y-v)^2}} \tag{1}$$

where $\mathbf{I}_1$ and $\mathbf{I}_2$ represent two consecutive images i and $i+1$ treated as matrices. The coordinates x and y

correspond to positions within the images. u and v are the integer displacement values applied to the x and y components of $\mathbf{I}_2$, respectively. The coordinates (u, v) that maximize the cross-correlation function NCC provide the best estimate for the displacement of a given subset. Implausible displacement results from the cross-correlation function, if present, are corrected by validating against neighbouring points, with deviations exceeding four times the neighbouring values replaced by interpolated values from surrounding nodes.

A quantitative comparison of the shear band thickness results, calculated from the axial, volumetric, and shear strain increments by Rattez et al. [41], indicated that the measured shear band size is not dependent on the deformation field chosen for the calculation. For the DIC analysis, the incremental axial strain field was calculated at intervals of every three images, corresponding to an approximate axial strain increment of 0.4%. Three cross-sections along the x- and y-axes were analysed by selecting points (1, 2, 3 in Fig. 5 (b)) located on the shear band. The deformation field in these sections was then interpolated using the least-squares method with a Gaussian equation (Fig. 5 (c) and (d)) [23]:

$$\Delta\varepsilon_{yy}(x_i) = A_i e^{-[(x_i - u_i)/V_i]^2} \tag{2}$$

where A_i denotes the amplitude; μ_i denotes the centre position, and V_i denotes variance of the Gaussian distribution. x_i represents the position along the x- or y-axis. The variance V_i , as shown in Fig. 5 (d), represents the Gaussian distribution's width at half its height, allowing the full width of the Gaussian distribution along a selected cross-section to be determined by [41, 42]:

$$w_i = 2\sqrt{2\ln(2)V_i} \tag{3}$$

The Gaussian distribution widths in the horizontal and vertical directions across the three cross-sections allow for the evaluation of the shear band width, w, for a specific cross-section using the relation:

$$w = \frac{w_x w_y}{\sqrt{w_x^2 + w_y^2}} \tag{4}$$

The overall shear band thickness at a particular time step is then determined by averaging the values obtained from the three points analysed, as shown in Fig. 5 (b).

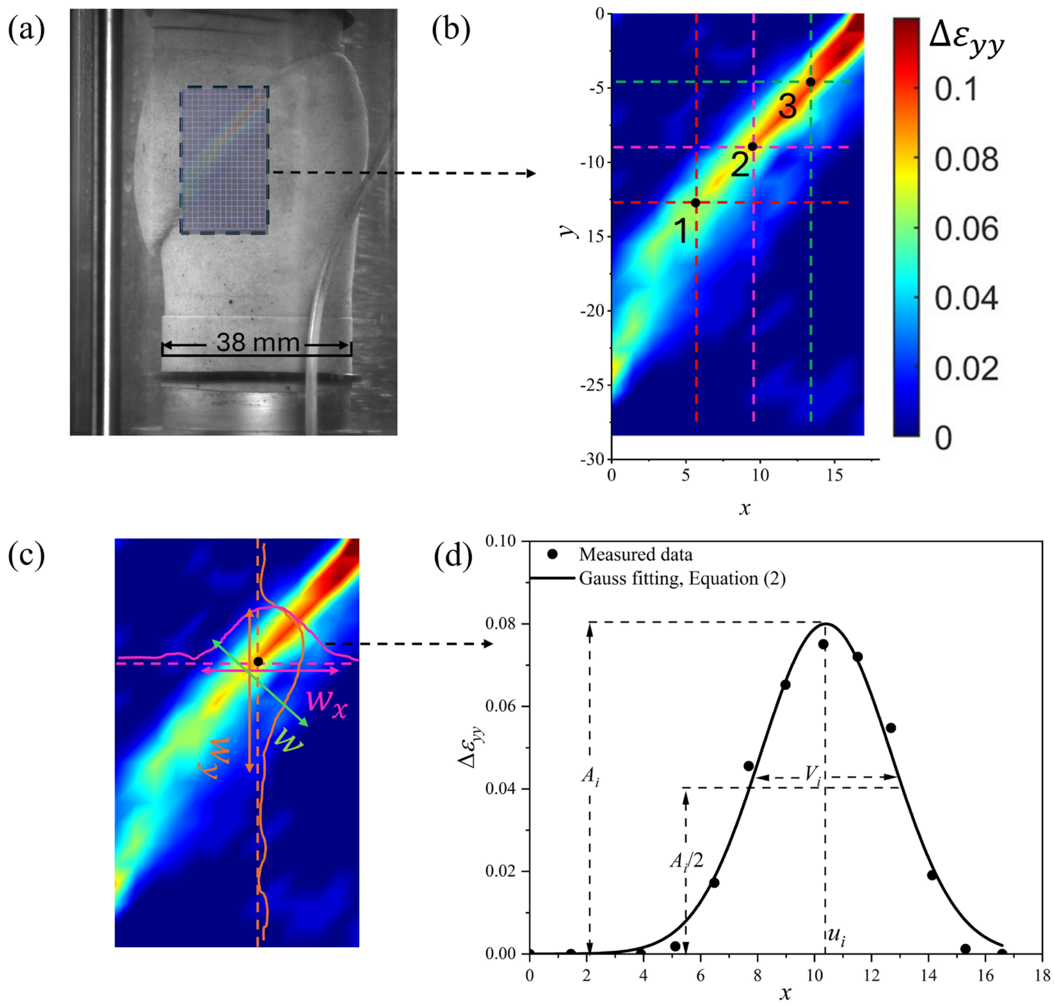

Fig. 5. Triaxial-DIC techniques: (a) Shear band captured by a camera, with the region of interest (dashed square window) and discretization mesh; (b) the incremental deformation field ($\Delta\varepsilon_{yy}$) derived from the window in (a), illustrating three measurement points and the corresponding vertical and horizontal cross-sections used for determining the shear band thickness; (c) a schematic representation of the procedure for calculating the shear band thickness using vertical and horizontal cross-sections and Gaussian fitting; (d) an example of Gaussian function fitting applied to the $\Delta\varepsilon_{yy}$ data for one selected cross-section.

3.2. DVC post-processing and shear band calculations

For each scan, 2400 radiographs were acquired at evenly spaced angular increments over a full 360° rotation, with each projection obtained by averaging three radiographs. The dataset was reconstructed into a 3D image volume using TESCAN's Panthera reconstruction software, which employs the Feldkamp-Davis-Kress (FDK) cone-beam filtered back projection algorithm for volumetric reconstruction [29]. A Shepp-Logan filter was applied within the algorithm to balance spatial resolution and noise amplification, while additional processing steps included ring artifact reduction and a post-reconstruction noise filtering (typically set to 0.2) to improve image quality. All the observations and quantitative analyses presented in this study are based on these greyscale volume datasets. Image processing for visualization was performed using Python and ImageJ. Displacement and strain calculations described in the following sections were conducted using the open-source software SPAM [56]. The approximation of shear band thickness is consistent with the method described in Section 3.1, based on deformation field.

3.2.1 Segmentation and three phase visualization

A binning factor of 2 was applied to the reconstructed greyscale CT images to downscale the resolution for more efficient histogram processing. A representative two-dimensional (2D) slice, taken at the midplane along the Z-axis, was extracted and visualized to provide a qualitative overview of the internal structure.

To characterize the material phases, namely NSS sand particles (coarser grains), silica fines, and voids, the grey level intensity distribution of the downscaled image was analysed by identifying characteristic peaks corresponding to each phase on the histogram. Histogram equalization [1] was then applied to enhance contrast, with the three main peaks normalized to 0.25, 0.5, and 0.75. This normalization enabled three-phase segmentation by applying threshold values at 0.375 and 0.625. Through histogram equalization, pixel intensity values were then redistributed to broaden the dynamic range and produce a flatter, more uniform histogram, thereby improving the visual separability of phases based on their greyscale values (Fig. 6 (b)).

Phase segmentation was subsequently performed based on the two threshold values, which separated the image into three distinct phases: low-density phase (voids), intermediate-density phase (silica fines), and high-density phase (NSS sand particles), as shown in Fig. 6 (c). Each phase was represented by a binary mask according to its assigned intensity range.

A median filter was applied to reduce isolated noise while preserving the integrity of phase boundaries to further improve the quality of the segmented images. Finally, a composite mixed-phase image was generated, wherein the intermediate- and high-density regions were combined and visually distinguished using different grey levels, as shown in Fig. 6 (d).

All processed images, including the original XZ plane, individual phase masks, and the mixed-phase composite, were saved in high resolution for visualization. Two-dimensional (2D) slices (specifically, the midplane along the Z-axis) were extracted and visualized to provide qualitative visualization of the evolution of the internal structure for Test 10 and Test11, as shown in Fig. 7.

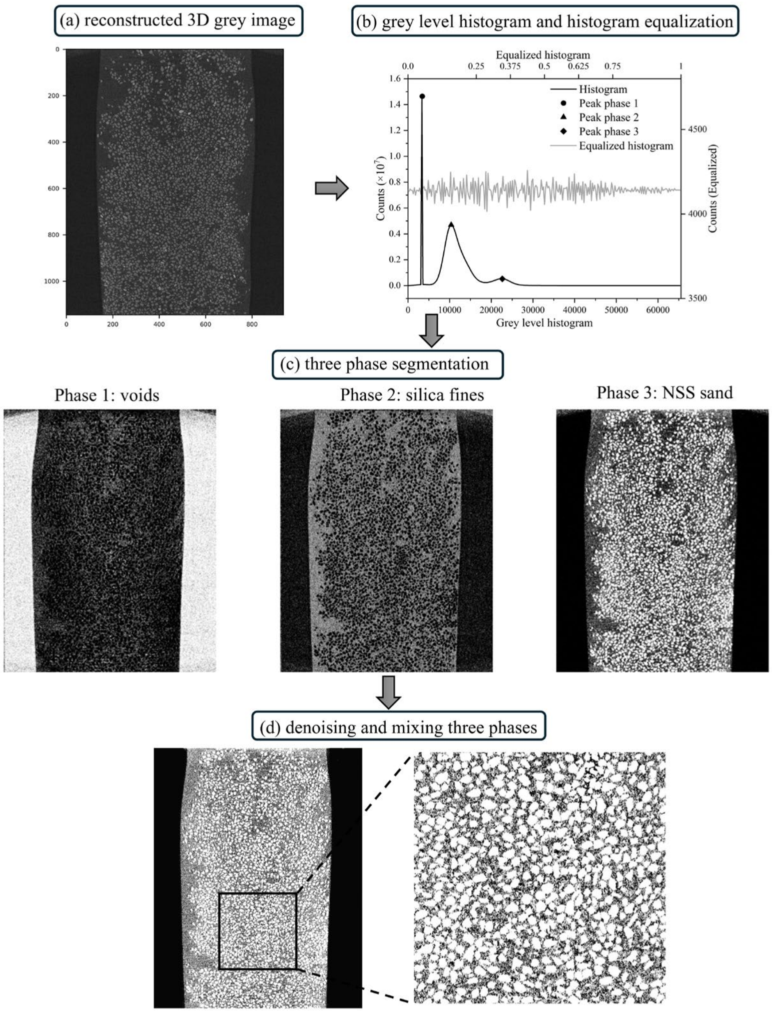

Fig. 6. Workflow for segmentation and three phases visualization.

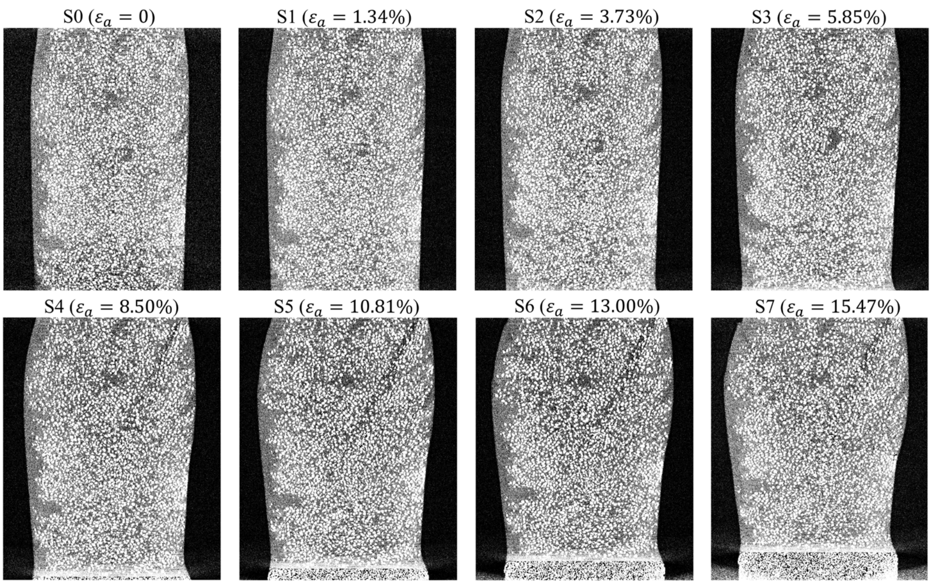

Fig. 7. Shear band formation and evolution from vertical 2D grey level slices (Test 11).

3.2.2 Calculation of displacement filed and strain tensor

Displacement measurements and strain calculations were conducted using the open-source software SPAM [56]. Regular grid local DVC was applied to each pair of consecutive images, corresponding to an approximate axial strain increment of 2.5%. The earlier image in each pair serves as the reference and the later image as the deformed image. A general workflow for how the various image correlation scripts are applied is illustrated in Fig. 8, with further details provided by Stamati et al. [56]. Convergence at corresponding steps were assessed using two criteria: (a) a maximum of 50 iterations, or (b) a norm of the change in deformation function$\| \delta\Phi \|$, smaller than 0.001.

The process starts with a non-rigid registration between two greyscale images to obtain an initial estimate of the deformation field, represented by a single linear and homogeneous deformation function, Φ_0. Eye-registration was only used as an initial step to roughly align the volumes. Specifically, if convergence is not achieved, a rigid eye-registration is applied to correct for misalignments in the z-direction using Φ_0, resulting in an updated transformation Φ_1. This is followed by a repeated registration step to compute a refined deformation function Φ_2.

Subsequently, a local non-rigid correlation and/or pixel search is conducted on a grid of regularly spaced measurement points defined in the reference image. Each of these points is the center point of a cubic correlation window. In this step, a sub-volume centred on each grid point in the reference image is matched to the deformed image using cross-correlation, evaluated through a brute-force search with a 1-pixel sensitivity, over a specific search range: for example, $(z_{min}, z_{max};\ x_{min};\ x_{max}; y_{min}, y_{max})$ = (-30, 30; -15, 15; -15, 15). For correlation, the grid spacing between the points is set to 20 pixels, with a correlation window of half window size 10 pixels. This corresponds to a physical window size of 600 μm (binning factor=2, voxel size=30 μm), which is slightly larger than the d_{100} of the NSS2. This selection minimizes the influence of window size while maintaining correlation effectiveness and efficiency. Since the shear band thickness of sand at residual state is approximately 10 to 20 times d_{50}, depending on the PSD, a minimum of 10 correlation windows are contained within the shear band [4, 5, 41, 63], which will be shown later in this section. Correlation is skipped in regions where the mean grey value of the window falls below a threshold (typically set to 12000 for most greyscale images), as these regions are identified as exterior to the sample.

It should be noted that for most of the scans, pixel search was found to be necessary as the deformation between two consecutive images is non-homogeneous and cannot be adequately captured by a single global deformation function Φ. The local displacements obtained from the pixel search define the final deformation field Φ_n. If some points fail to converge, interpolation is used to fill in missing values and produce a complete displacement field.

DVC analysis was completed by determining the strain tensor. A finite strain tensor U, along with its first two invariants-the volumetric strain U_{vol} and deviator strain U_{dev}, are calculated from the local displacement filed defined by Φ_i:

$$U = U_{vol} \cdot U_{dev} \tag{5}$$

$$U_{vol} = J^{1/3} \times I \tag{6}$$

$$U_{dev} = \frac{1}{J^{1/3}} \times U \tag{7}$$

where J is the determinant of the strain tensor, and I is the identity matrix.

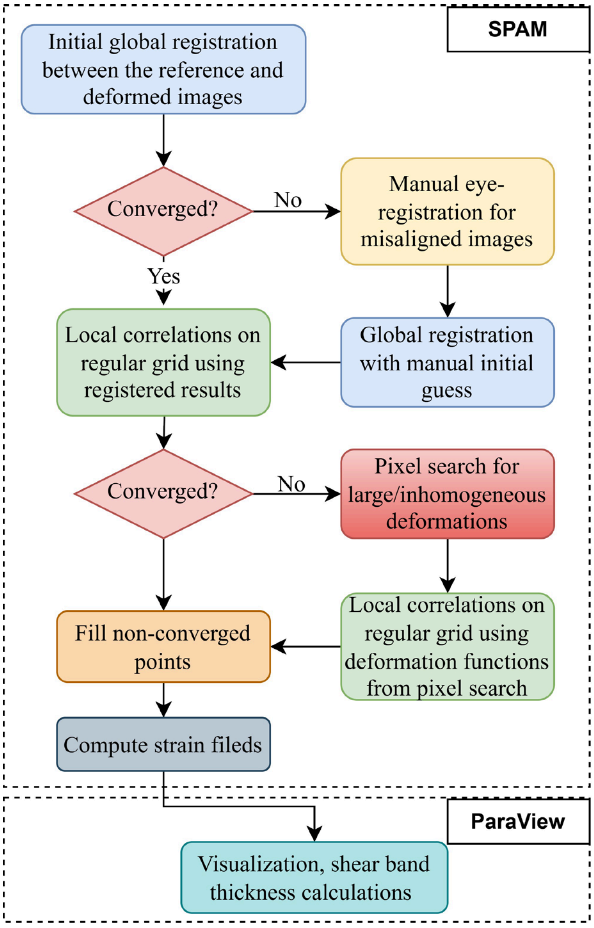

Fig. 8. Workflow diagram for DVC analysis using SPAM and shear band thickness analysis and visualization using ParaView.

The visualization and analysis of the shear band based on the strain field were performed using the open-source software ParaView. As the X-ray CT scanning is applied on a cubic volume, a lower strain threshold of 10^{-5} is applied to exclude regions outside the sample boundaries, allowing clear visualization of the strain field within the sample volume, as shown in Fig. 9 (a) and (b). For Tests 10 and 11, the deviator strain field was selected to visualize and analyze shear band evolution and to measure shear band thickness measurements, as it provides higher average strain values and clearer contrast. This choice does not influence the measured thickness of the shear band [41].

Additional lower and upper strain thresholds were applied to isolate the shear band, as illustrated in Fig. 9 (c). These thresholds were individually calibrated for Test 10 and Test 11 but held constant across all incremental strain fields within each test to ensure consistency in shear band visualization. A transparency coefficient of 0.5 was applied to the full strain field, upon which the isolated shear band was overlaid (Fig. 9 (c)).

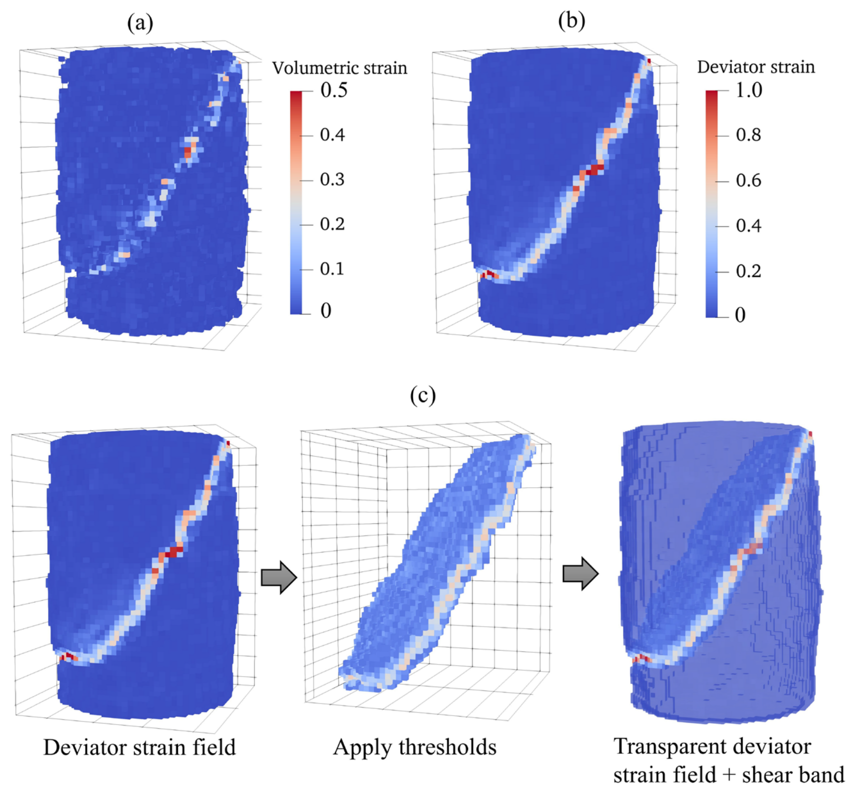

Fig. 9. Visualization of shear band development based on strain fields: (a) volumetric strain filed; (b) deviator strain field; (c) deviator strain field with shear band highlighted.

Once the deviator strain field and a clear view of the shear band were obtained, a strike is drawn along the shear plane, and slices perpendicular to it were extracted, as shown in Fig. 10 (a) and Fig. 10 (c). In this study, three slices were taken for each strain field, and three measure points were selected in the middle of the shear band for thickness approximation. The thickness was calculated using the same method described in Section 3.1 for DIC, where points along the shear band (Fig. 10) were used to extract strain profiles, and the shear band thickness was approximated by fitting a Gaussian curve to the strain distribution in horizontal and vertical direction. For Test 11, where multiple shear bands developed, two sets of measurement points were used to determine the thickness of each band, as shown in Fig. 10 (d). It should be noted that in Fig. 10 (c), some regions near the bottom exhibit excessively large strains and failed to correlate successfully (a limitation also encountered by others, e.g., Desrues et al., [18]), however, this does not affect the measurement of shear band thickness. Fig. 11 shows the effect of DVC half window size on deviator strain measurement. In Fig. 11 (a), the 5-pixel window produces a noisy field, while 40-pixels yield a smooth but less detailed band. The 10-pixel case provides a clear and continuous shear band, balancing resolution and stability. In Fig. 11 (b), strain profiles extracted along the marked line confirm that the 10- and 40-pixel results follow Gaussian distributions, with a variance difference (V_i= 61.82 and 61.93, respectively) of less than 0.18% and high R^2 values. Considering both resolution and stability, a half window size of 10 pixels was adopted in this study.

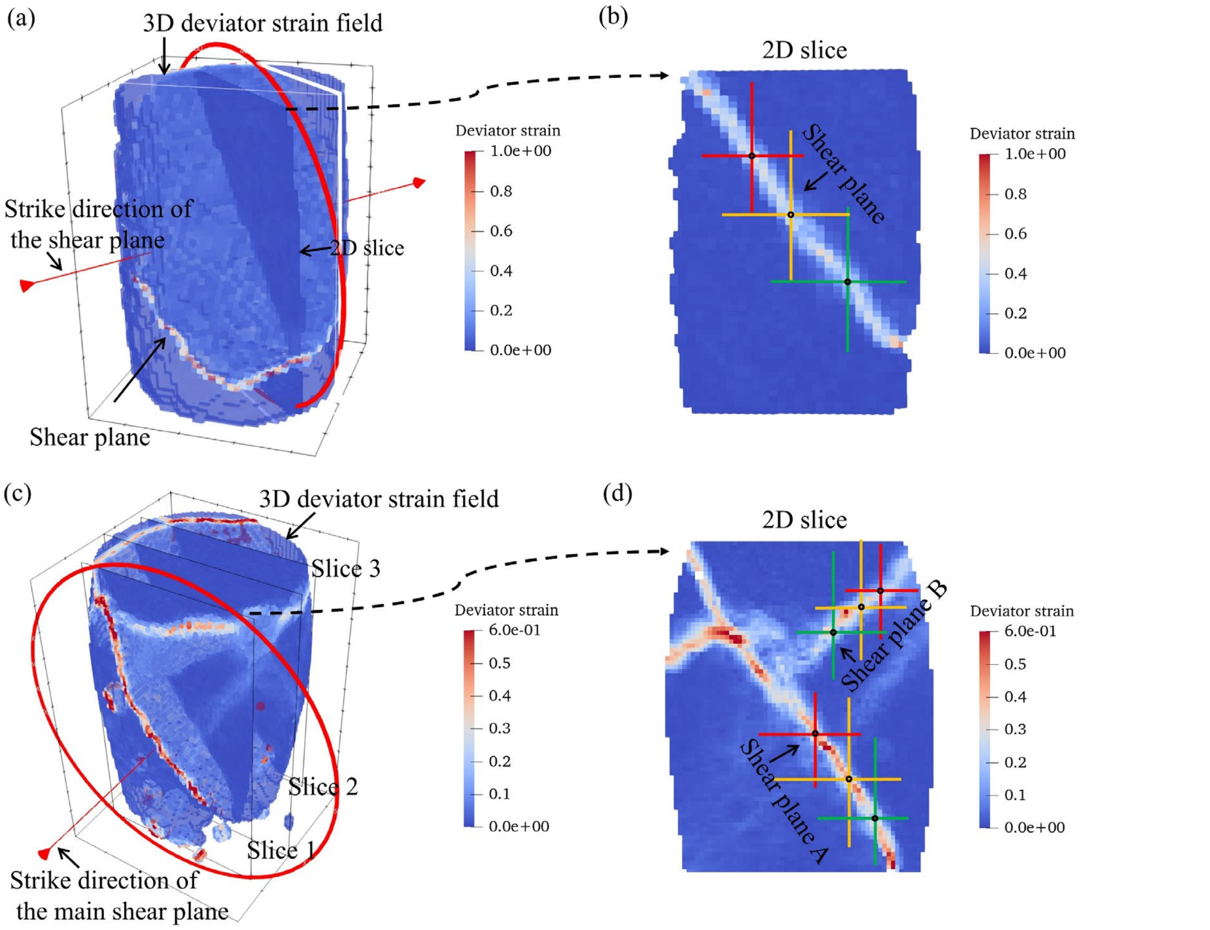

Fig. 10. Illustration of the measurements of shear band thickness from DVC results: (a) selection of a representative 2D slice from the 3D deviator strain field (Test 10, S5-S6); (b) three measurement points on shear band in the extracted 2D slice; (c) selection of a 2D slice from the 3D deviator strain field showing multiple shear planes (Test 11, S5-S6); (d) measurement points for two shear bands in extracted 2D slice.

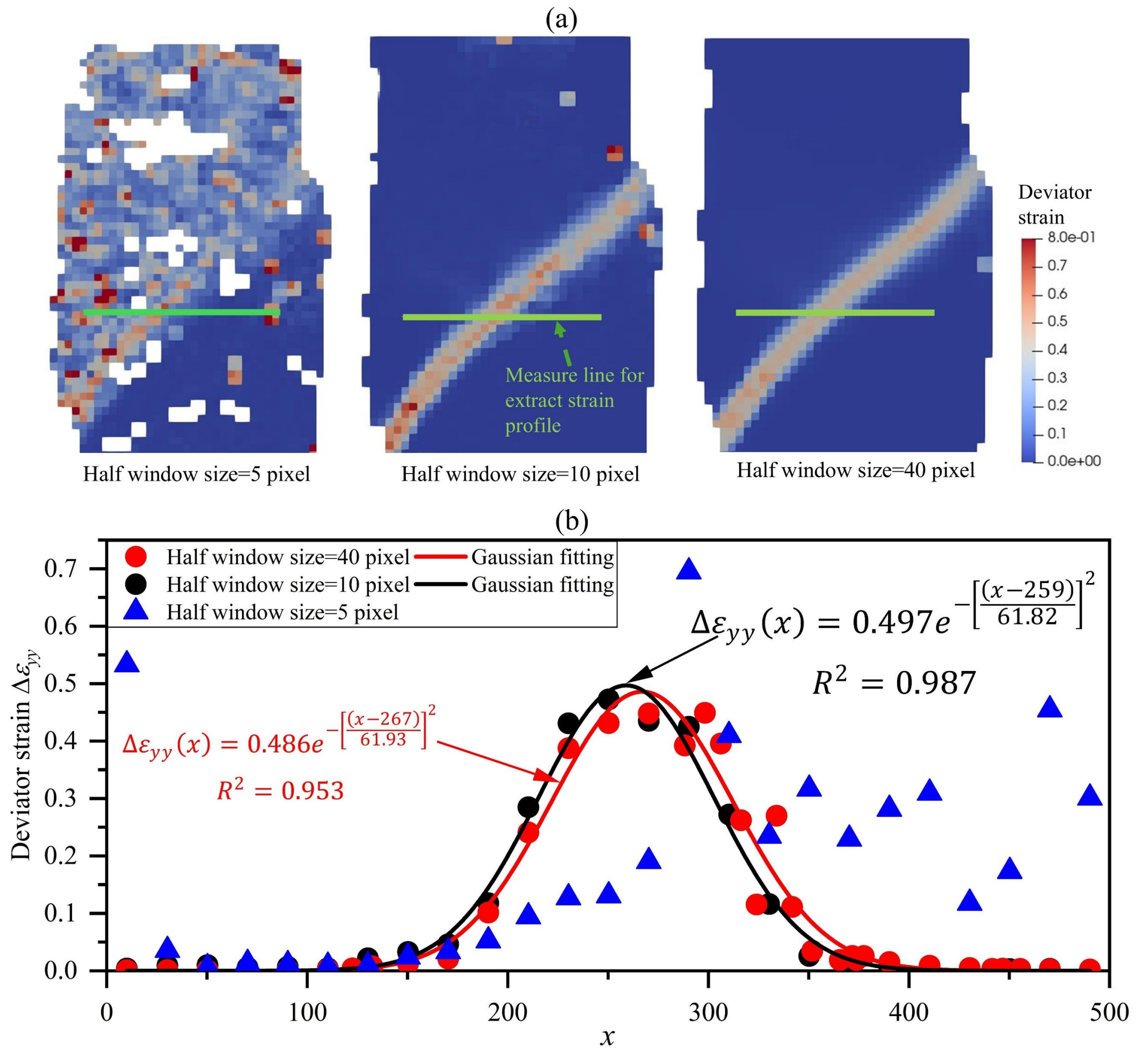

Fig. 11. Effect of DVC half window size on strain measurement and Gaussian fitting. (a) 2D slices of deviator strain fields obtained with half window sizes of 5, 10 and 40 pixels, with the green line indicating the location for extracting strain profiles; (b) deviator strain profiles along the selected line for different half window sizes, together with their Gaussian fits.

4. Results

4.1. Stress-strain results

In this study, the triaxial test results are presented using conventional triaxial $p' - q$ notations: mean effective stress $p' = (\sigma_1' + 2\sigma_3')/3$ and deviator stress $q = \sigma_1' - \sigma_3'$; axial strain $\varepsilon_a = 100\Delta l/l_0$ and volumetric strain $\varepsilon_v = -100\ln{(V/V_0)}$, where σ_1' and σ_3' are principal effective stresses, Δl and l_0 are the change in sample length and the initial sample length prior to shearing, and V and V_0 are the current and the initial sample volume. The friction angle $\emptyset$ is given by $\sin\emptyset = \frac{\sigma_1'-\sigma_3'}{\sigma_1'+\sigma_3'}$.

4.1.1 Triaxial-DIC stress-strain responses

Fig. 12 plots the stress-strain responses from Tests 1-9, and Fig. 13 plots the friction angles at peak and residual strength conditions as a function of d_{50} and fines content. For the samples composed 100% NSS, but with different d_{50} (Test 1-3, Fig. 12 (a) and (b) and Fig. 13 (a)), the initial stiffness, peak deviator stress (ranging from 772 to 806 kPa), peak friction angle, residual strength (ranging from 485 to 507 kPa at 22.5% axial strain) and residual friction angle are generally similar and comparable. A slight decreasing trend in peak and residual strength and friction angles is observed with increasing of d_{50}, similar to Rattez et al [41]. Notably, Test 1 and Test 2 exhibit strain-softening followed by an asymptotic approach to a constant deviator stress, whereas Test 3 (coarser NSS, 425-600 μm) continues to soften beyond the peak. This difference is attributed to the link between strain softening and the formation of a dominant shear band [11, 17, 41]: Tests 1 and 2 developed a dominant and well-defined shear band, while Test 3 consistently showed a bulging-type failure in repeated tests without a dominant shear band. The volumetric strain exhibits similar behaviour at small strains (<2%), after which dilation becomes more pronounced with increasing particle size.

For the samples with varying fines content but similar d_{50} (Test 2, 4-7), the peak deviator stress increases with fines content up to 20%, consistent with experimental findings by Salgado et al. [48], Carraro et al. [14], Chang and Yin [15] and Xiao et al. [67]. However, when the fines content exceeds 20%, up to 40% in this study, the peak deviator stress decreases with further increases in fines content, in agreement with experimental results by Vallejo [61] and numerical simulations by Zhu et al. [71] and Sufian et al. [57]. Some experimental [68] and numerical studies [2, 57] have shown that the threshold fines content may vary and depends on the particle size ratio between coarse and fine fractions. A similar trend is observed in residual stress and friction angle.

The effect of cohesionless fines on volumetric strain under shearing remains somewhat contradictory in the literature. Some studies have reported that the addition of fines increase dilation for dense silty sand, e.g., Salgado et al. [48] and Carraro et al. [14]; others found that fines reduces the dilation behaviour, e.g., Yilmaz et al. [68]. The volumetric strain at residual state ($\varepsilon_a > 20\%$) in this study generally decreases with increasing fines content in agreement with Yilmaz et al. [68].

For the samples with 20% of fines content but different d_{50} (Test 8, 5 and 9), the peak deviator stress and friction angle increases with d_{50}, or $d_{50\,coarse}/d_{50\,fine}$, which is 5.19, 7.98 and 11.3 for Test 8, 5 and 9, respectively. Similarly, Yilmaz et al. [68] reported a slight increase in peak deviator stress for silica sand mixtures containing 20% fines, with comparable $d_{50\,coarse}/d_{50\,fine}$ of 4.52, 7.93 and 11.93. The increase in this size ratio appears to enhance both compressive and dilative behaviour, consistent with the observations by Yilmaz et al. [68]. The dilation at large strain increases with d_{50}.

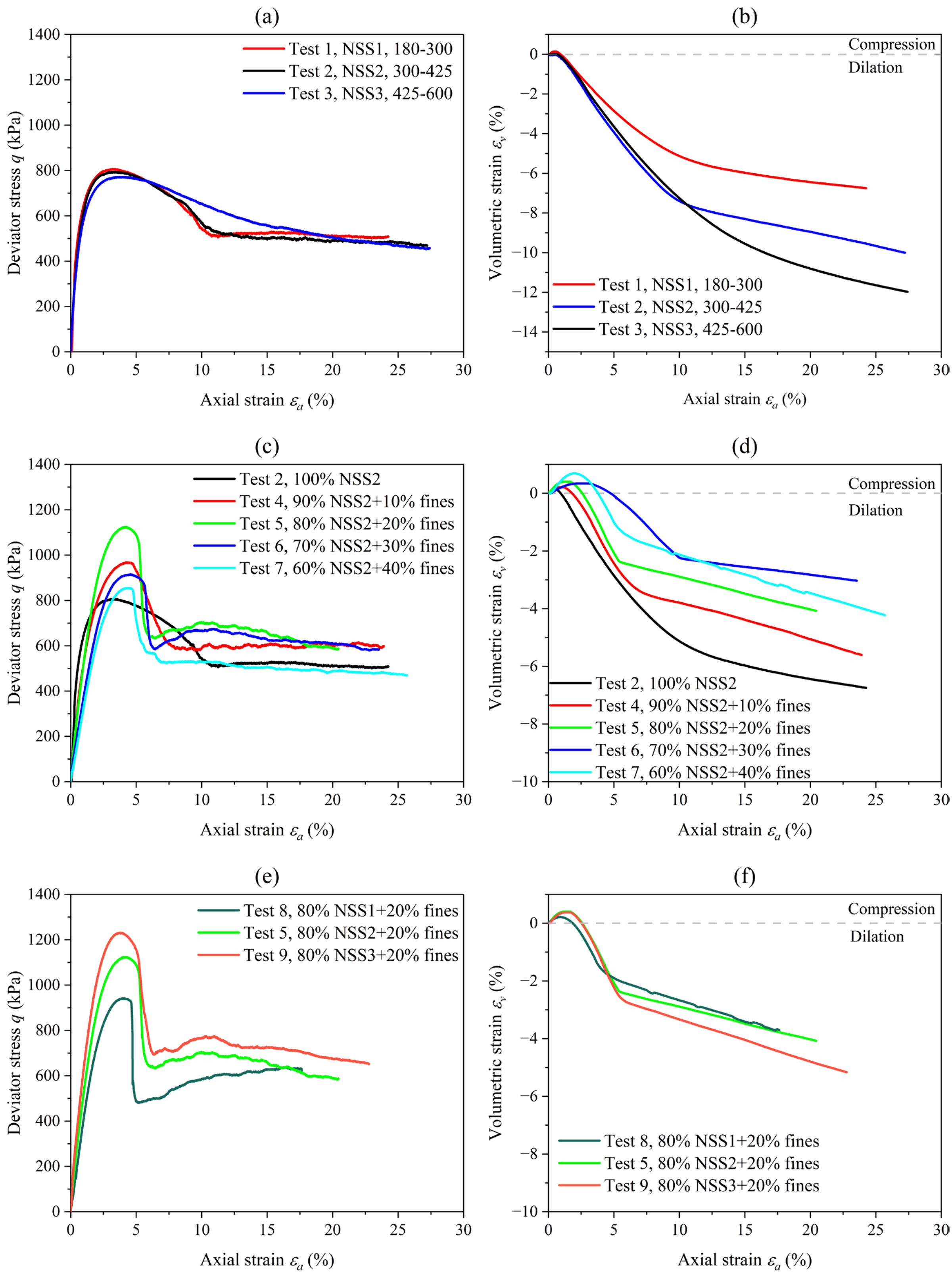

Fig. 12. Stress-strain and volumetric strain responses from Triaxial-DIC tests (Test 1-9). (a), (b): NSS1, NSS2, and NSS3; (c), (d): NSS2 with varying fines content; (e), (f): NSS1, NSS2 and NSS3 with 20% of fines content.

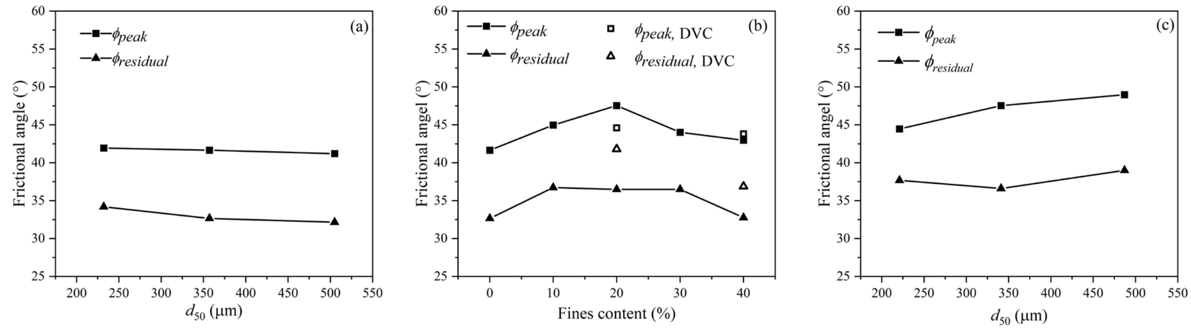

Fig. 13. Friction angles at peak and residual strength conditions plotted as a function of (a) d_{50} for Test 1-3 (without fines); (b) fines content for Test2, 4-7, and Test 10 and 11 from Triaxial-DVC (similar d_{50}); (c) d_{50} for Test 5, 8 and 9 (with same fines content of 20%)

4.1.2 Triaxial-DVC stress-strain responses

Fig. 14 shows the deviator stress plotted against axial strain for Test 10 and 11 obtained from triaxial shearing with *in situ* X-ray CT scanning, alongside the results from Test 5 and Test 7 obtained using Triaxial-DIC, for comparison. The repeated, evenly spaced drops in deviator stress reflect stress relaxation that occurred during the loading pauses prior to each X-ray scan, ensuring that relaxation during scanning was avoided. The labels near each stress drop mark the sequential scanning points. Both curves exhibit strain-softening behaviour after reaching the peak strength: the deviator stress in Test 10 oscillates around a constant residual stress value once ε_a exceeds about 7%, whereas in the Test 11, it continues to decline until the end of the test, attributed to the continuous development of multiple shear planes within the sample. The friction angles at peak and large strain (i.e., ε_a>15%) for Tests 10 and 11 are shown in Fig. 13. The discrepancies in stress compared to the Triaxial-DIC results may be attributed to differences in sample size and the inherent uncertainty of soil behaviour.

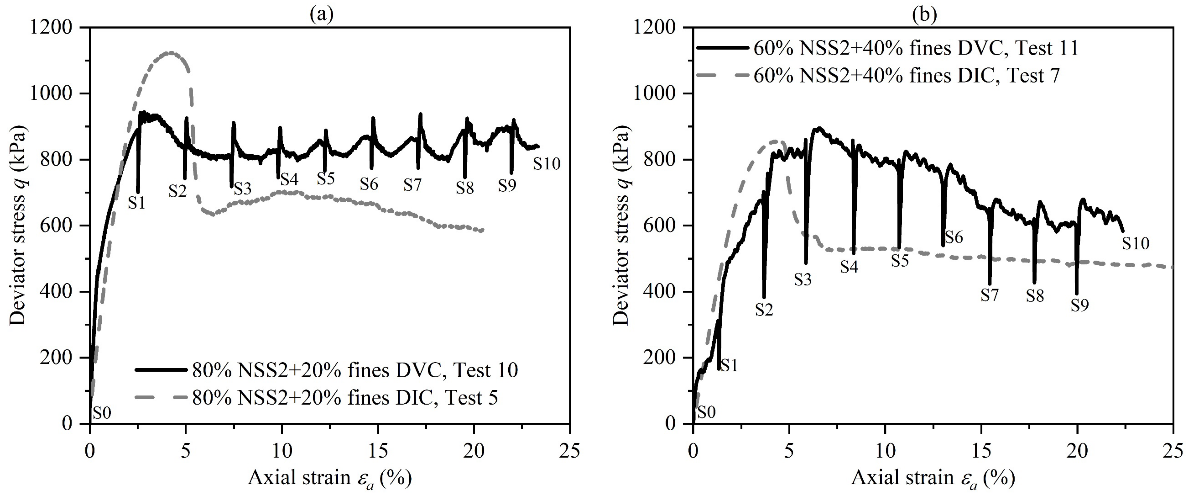

Fig. 14. Deviator stress plotted against axial strain for triaxial tests with DVC.

4.2. Shear band evolution and thickness measurements

4.2.1. Shear band evolution

Fig. 15 shows the captured images at different axial strains for Test 5 (80% NSS2 and 20% fines) and the corresponding strain field resulted from DIC. Fig. 16 presents the deviator strain field for Test 10 (80% NSS2 and 20% fines), illustrating the development and evolution of the shear band based on DVC results. Fig. 17 compares the development and evolution of shear bands in a sand mixture comprising 60% NSS2 and 40% fines, as observed in Test 7 (Triaxial-DIC) and Test 11 (Triaxial-DVC), at various levels of axial strain.

In Test 5, a distinct shear plane is observed at 5.8% axial strain, while in Test 10, it is captured at 5%. These axial strain values correspond to the points where strain-softening ends and the deviator stress transitions to a more stable, residual state, as shown in Fig. 14 (a). From Fig. 15 (b), relatively homogeneous deformation throughout the observation window is observed at 2.5% axial strain, corresponding to 87.8% of the peak strength. Desrues et al. [18], using Triaxial-DVC with intensive scans at 0.5% axial strain intervals, reported the formation of multiple shear planes as early as 96% of the peak strength during the pre-peak stage. It is noted that the strain localization along the shear band is not uniform during its initiation, as shown in Fig. 15 (b) at ε_a=5.8%, where a higher concentration of strain is observed in the upper section.

In comparison, the DVC results in Fig. 16 show relatively higher strain localization scattered within the sample at ε_a=2.5%, indicating the early signs of shear band formation. A similar pattern is observed in the Triaxial-DIC and Triaxial-DVC comparisons for sands comprising 40% fines (Fig. 17 (b) and Fig. 17 (c) at ε_a=5.85%. This internal strain development cannot be captured by Triaxial-DIC, which is limited to surface deformation on the membrane. Notably, after a clear primary shear plane develops, a secondary shear plane begins to form at ε_a=12.5% (Fig. 16). This becomes more pronounced in the sand with 40%, where multiple shear bands are clearly captured at ε_a=13% Fig. 17 (c) (also see Fig. 10 (c) and Fig. 10 (d)).

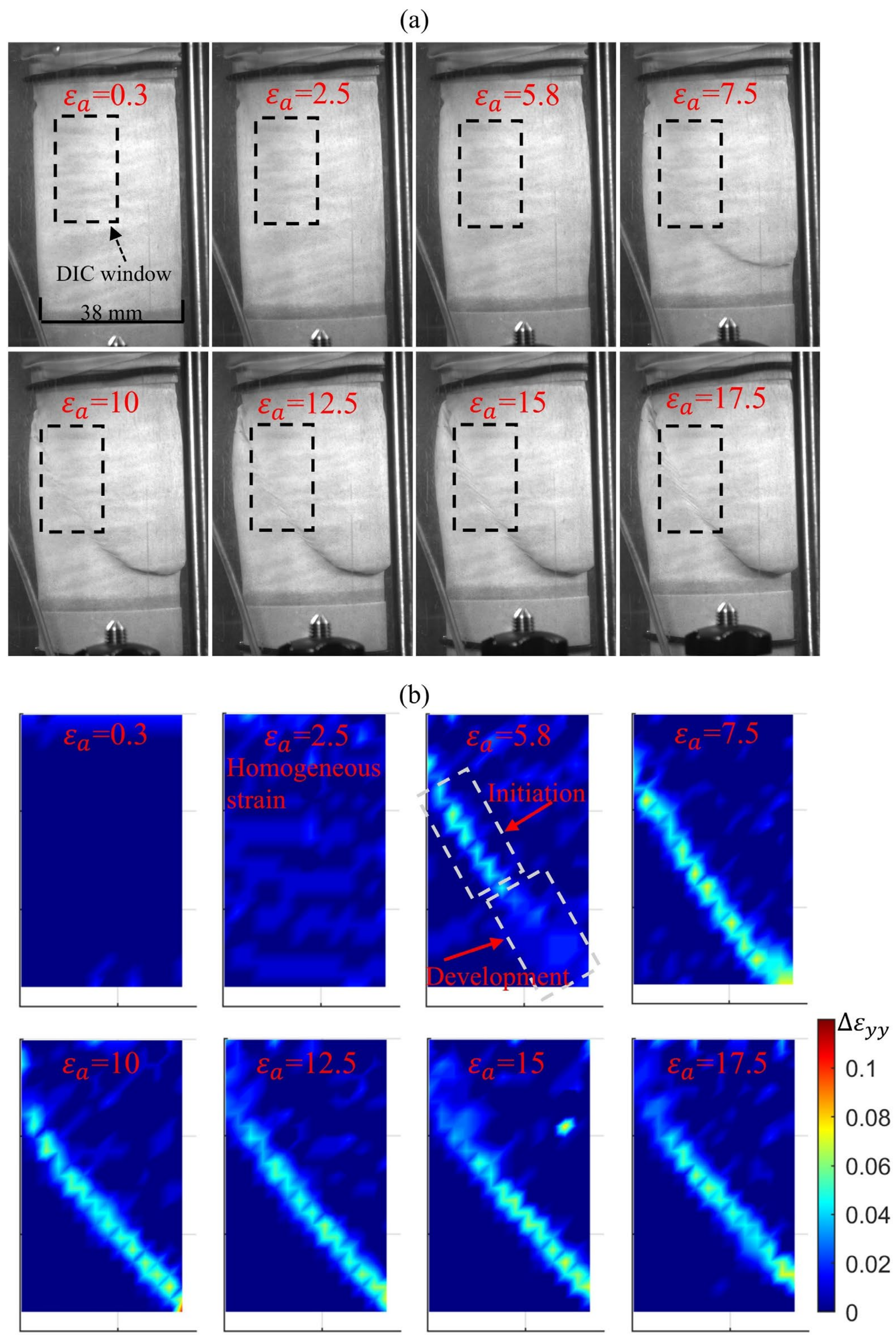

Fig. 15. Shear band evolution for Test 5 (80% NSS2 and 20% fines) from Triaxial-DIC (a) Captured images at different axial strains; (b) strain field computed within the DIC window, illustrating the development of the shear band

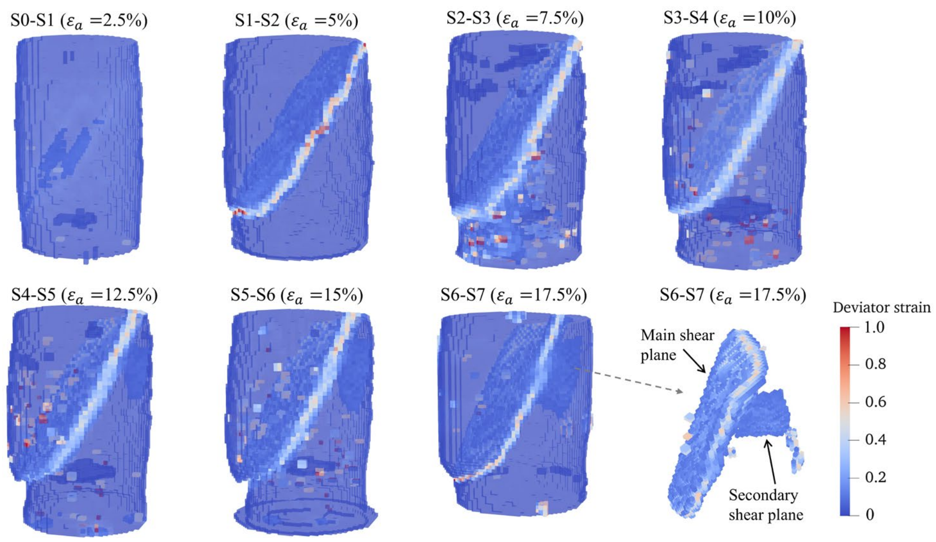

Fig. 16. Shear band formation and evolution obtained from the deviator strain field: Triaxial-DVC results of Test 10 (80% NSS2 and 20% fines).

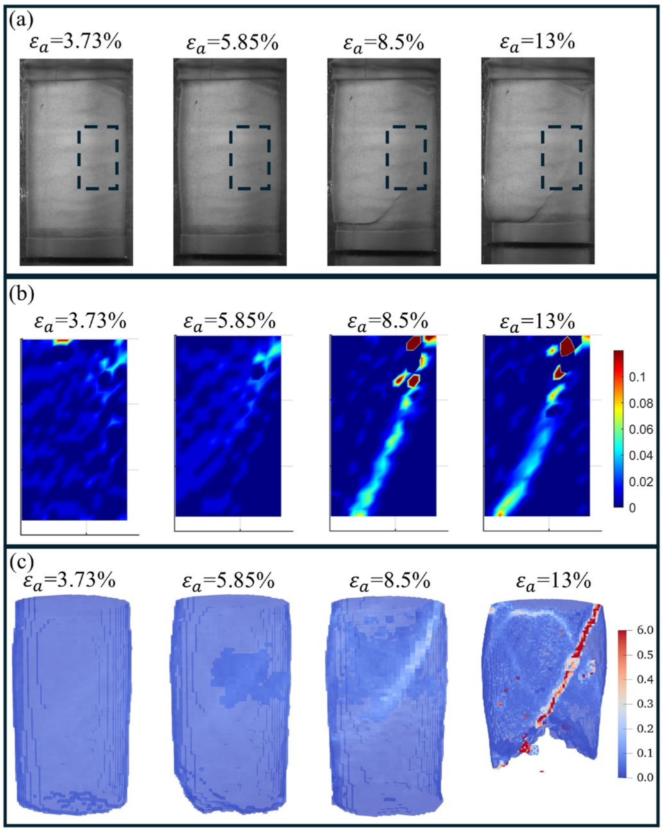

Fig. 17. Comparison of the development and evolution of shear bands in a sand mixture comprising 60% NSS2 and 40% fines, as observed in Test 7 (Triaxial-DIC) and Test 11 (Triaxial-DVC) at different axial strain levels. (a) Triaxial-DIC images; (b) Strain fields obtained from Triaxial-DIC; (c) Strain fields obtained from Triaxial-DVC.

Fig. 18 shows a comparison of the evolution of residual shear band thickness measured using Triaxial-DIC (Test 5) and Triaxial-DVC (Test 10) for samples containing 80% NSS2 and 20% silica fines. Both measurement methods yield similar mean values, i.e., 3.408 mm for DIC and 3.420 mm for DVC, indicating only a minor difference in the estimation of shear band thickness. The DVC data exhibit slightly lower variability (variance=0.0244) compared to DIC (variance=0.0352), suggesting that DVC provides more consistent internal measurements. This result is obtained under conditions the ratio of the area of an individual mesh between DIC and DVC is 3.8:1, closely matching the ratio of the sample's vertical cross-sectional areas (3.6:1). Nonetheless, the overall agreement between the two methods confirms the reliability of surface-based DIC in capturing shear band thickness, especially in cases where 3D internal imaging may not be feasible.

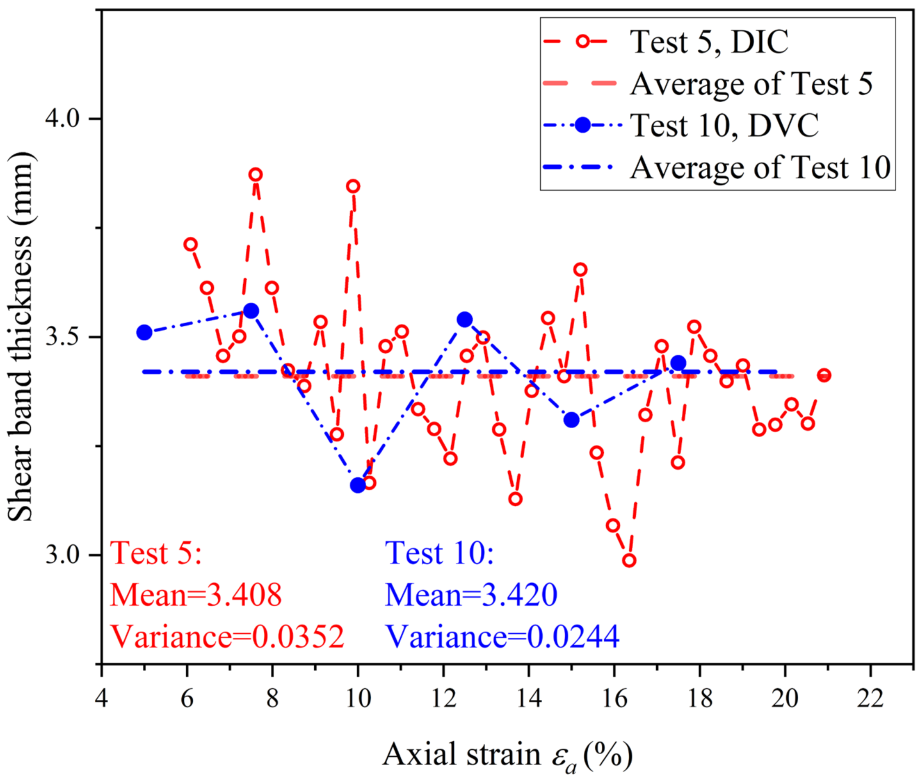

Fig. 18. Comparison of residual shear band thickness measured using Triaxial-DIC and Triaxial-DVC for samples containing 80% NSS2 and 20% silica fines.

4.2.2. Residual shear band thickness

Fig. 19 (a) presents the measured residual shear band thickness of NSS2 with varying fines content, together with the ratio of this thickness to that of pure NSS2, plotted against the fines content. A general increasing trend is observed, with shear band thickness growing as fines content increases under similar d_{50} conditions. For fines content ranging from 0-40%, the trend is best described by a linear relationship with R^2=0.761. It is worth noting that the secondary shear band (shear plane B in Fig. 11 (d)) observed in Test 11 using Triaxial-DVC appears slightly thicker than both the main shear band and the thickness measured using Triaxial-DIC. The authors attribute this to the secondary shear band still being in the process of development. As the fines content increases from 0% to 40%, the ratio of the residual shear band thickness of NSS2 with fines to that of pure NSS2 increases from approximately 1.0 to 1.3. Fig. 19 (b) shows a comparison of residual shear band thickness plotted against d_{50} of NSS sand, both with and without the addition of 20% of fines. The residual shear band thickness increases with d_{50}, in agreement with others [41, 46]. The addition of fines leads to a slight reduction in d_{50} and a corresponding increase in residual shear band thickness. For pure NSS3 (400-625 μm), no distinct shear band was observed through visual inspection during triaxial shearing tests on samples with diameters of 38 mm and 20 mm. However, the addition of 40% fines significantly altered the deformation behaviour, as evidenced by the formation of multiple shear bands.

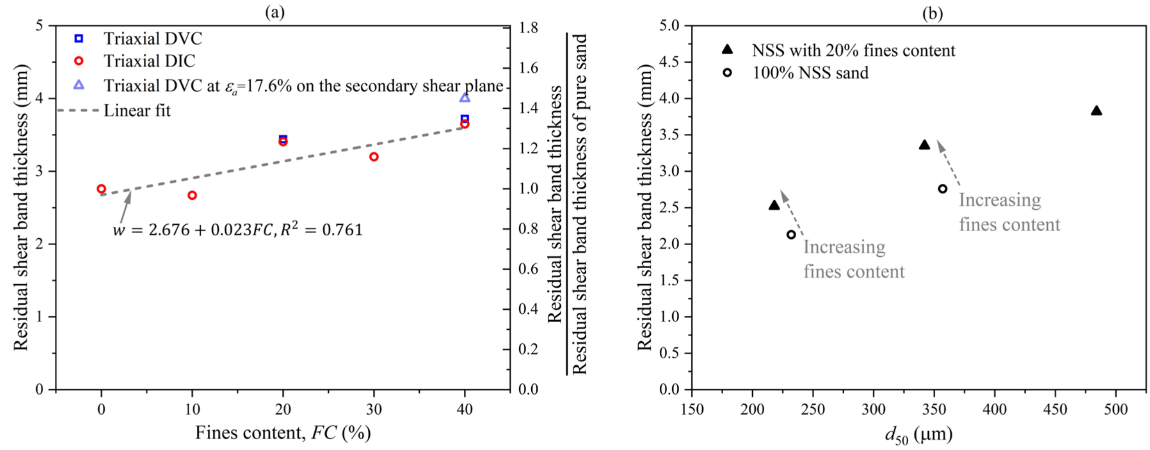

Fig. 19. (a) residual shear band thickness plotted against fines content; (b) residual shear band thickness plotted against d_{50}

Fig. 20 summarizes the relationship between the residual shear band thickness normalized by d_{50}, mean particle size d_{50}, and fines content. For samples with 0% and 20% fines content, the normalized shear band thickness decreases with increasing d_{50}, as shown in Fig. 20(a). This trend aligns with the experimental observations by Alshibli and Sture [5] and the discrete element method (DEM) simulation by Guo [24]. The addition of fines (from 0-20%) leads to an increase in normalized shear band thickness.

Data points in Fig. 20(b) include results from both Triaxial-DIC and -DVC measurements for NSS2 with varying fines contents, as well as samples with fixed (or zero) fines content and different d_{50}. Regardless of the coarse fraction's particle size, a general increasing trend is observed, with the normalized shear band thickness rising approximately 7.6 to 11.66 as the fines content increases. The trend can be represented by a linear fit, with a coefficient of R^2=0.575. Despite a moderate R^2, the relationship between fines content and normalized residual shear band thickness is statistically significant (with significance p=0.00687 and F-statistic=12.15), indicating that the fitted slope is unlikely to arise from random variation. This trend suggests that increasing fines content broadens the normalized shear band thickness.

It is worth noting that these observations are consistent with previous studies on the shear band thickness in sands with uniform and well-graded PSD. Rechenmacher et al. [46] observed that shear band thickness in uniform sands typically ranges from 6-9 d_{50}, increasing slightly to 8-9.5 d_{50} in well-graded sands, which can be interpreted as the effect of increasing fines across a range of consecutive smaller sizes. Rattez et al. [41] further confirmed this trend, reporting shear band thicknesses of 9-14 d_{50} for uniform sands and 14-20 d_{50} for well graded sands. These findings highlight that increased gradation in particle size tends to result in wider shear bands.

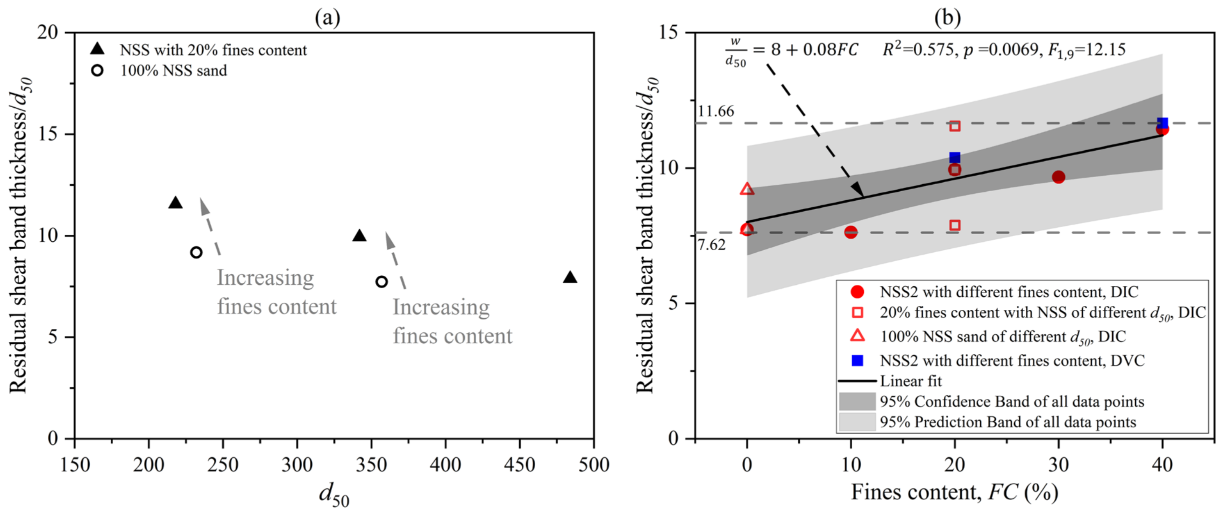

Fig. 20. Normalized shear band thickness: (a) the ratio of residual shear band thickness and d_{50} plotted against d_{50}; (b) the ratio of residual shear band thickness and d_{50} plotted against fines content

5. Discussion

5.1 Comparison of DIC and DVC for shear band thickness evaluation

A series of triaxial tests with digital image correlation (DIC), along with in situ mini-triaxial tests with digital volume correlation (DVC), have been performed on dense sands with varying fines content to investigate the effects of fines content on shear band thickness. The mechanical behaviour of the mixed sands was consistent with trends reported in the literature: both the peak deviator stress and peak friction angle increased with fines content up to 20%, beyond which both parameters decreased with further addition of fines. For the samples containing 20% fines but differing in mean particle size, both the peak deviator stress and peak friction angle were found to increase with increasing mean particle size. The mechanical responses observed from Triaxial-DIC and Triaxial-DVC were generally comparable, with both sets of tests exhibiting strain-softening behaviour following similar peak deviator stresses reached at similar axial strains.

The measurements of shear band thickness using DIC and DVC were compared in this study. The results show that the shear band thickness measured from both methods exhibit close values, validating the effectiveness of approximating shear band thickness using surface displacement information captured from membrane's speckle pattern. However, each method has its advantages and limitations. Triaxial-DIC method uses high-resolution cameras, together with a conventional triaxial apparatus, to capture continuous changes in the speckle pattern applied to the sample membrane. Accurate DIC measurements require careful control of lighting conditions (e.g., consistent exposure, minimal reflection, and optimal camera angles to reduce distortion), as well as slow displacement rates and short shutter speeds. Once the imaging system is initiated, no interruption of the loading process is necessary, allowing for automatic and undisturbed image acquisition. The short imaging interval (e.g., 30 seconds in this study) enables the collection of a large number of sequential images from multiple angles (typically 240 per angle for one test). The DIC analysis is based on 2D surface data, making it computationally efficient and relatively straightforward compared to DVC. Additionally, both open-source and commercial DIC software packages are widely available. The quality of DIC results depends heavily on the speckle pattern size, camera resolution, and lighting conditions [16, 20, 41, 47].

In contrast, the Triaxial-DVC method is more technically complex, more time consuming, and cost intensive. It requires a specially designed mini-triaxial apparatus that fits within an X-ray CT scanner, as well as a compatible loading frame. Prior to each in-situ X-ray CT scan, the loading must be paused to allow the sample to reach stress equilibrium, which introduces slight disturbances in the smoothness of the stress-strain curves. Each scan takes a considerable amount of time (e.g., 26 minutes in this study with a voxel size of 15 μm), and a typical DVC test in this study involves 10 scans over 10 hours. This represents a trade-off between the number of scans and the incremental strain between them to ensure both practical feasibility and adequate spatial resolution. For higher-resolution scans with smaller strain intervals, aimed at improving the convergence rate in correlation calculations, the scanning duration can extend to several working days [6, 40, 66]. Before DVC processing, extensive 3D image reconstruction and preprocessing are required, including histogram analysis, segmentation, denoising, and phase combination (as shown in Fig. 6). The DVC analysis itself is computationally demanding and highly sensitive to image quality and resolution. As demonstrated in Fig. 9, the accuracy of the DVC output depends on both the sample size and the ability to resolve individual grains and local strains between image pairs [7]. Nevertheless, Triaxial-DVC provides full-field 3D displacement and strain measurements throughout the sample volume, capturing internal deformation that is inaccessible to surface-based DIC. This makes DVC particularly valuable for investigating strain localization patterns, internal shear band development, and micro-mechanical mechanisms in granular materials. While more complex and resource-intensive, DVC complements DIC by providing insights that enhance the understanding of the internal structure and evolution of deformation, especially in cases where surface observations alone may be insufficient (for example when multiple shear planes develop).

Rattez et al. [41] proposed Gaussian distribution fitting of the strain field obtained from Triaxial-DIC to approximate shear band thickness. This study extends that approach to the three-dimensional strain field derived from Triaxial-DVC. The combined use of DIC and DVC to measure shear band thickness during triaxial shearing is demonstrated here for the first time. One original contribution of this combined approach is that the DVC results validate the effectiveness of approximating shear band thickness based on surface displacement data. Previous research have established that shear band thickness scales with the mean particle size d_{50} [4, 5, 6, 23, 26, 35, 41, 55, 62]. The findings of this study have extended that knowledge by demonstrating that both absolute and normalized shear band thickness increase with fines content. Moreover, the presence of fines fundamentally alters the deformation behaviour, even in samples that initially do not exhibit distinct shear bands.

The normalized shear band thickness was found in the range of 7.62 to 11.66 d_{50}, which agrees with previous quantitative investigations of the effect of PSD on shear band development and measurement [41, 46]. Uniquely, this study quantifies the influence of fines content on both absolute and normalized shear band thickness through Triaxial-DIC and Triaxial-DVC.

5.2 Shear band thickening due to increase in fine content

Combining Triaxial-DIC and Triaxial-DVC also enables a mechanistic interpretation of how increasing fines content leads to a thickening of the shear band. A schematic illustration from macro-, meso-, and micro-scale perspectives is presented in Fig. 21. Fig. 21 (a) shows a representative macroscopic stress-strain response from triaxial shearing, annotated with the three-stage strain localization and shear band formation framework proposed by Tordesillas [59] based on DEM simulations. Stage 1 is characterized by homogeneous (affine) deformation and rapid linear stress increasing. In Stage 2, strain localization initiates through non-affine motion accompanied by mesoscale features such as microbands, although rearrangements remain local. Force chains form without buckling until shear banding begins near peak stress. Stage 3 corresponds to the development and persistence of a fully formed shear band, where buckling of force chains drives unjamming-jamming cycles, and large dilatation.

Experimental and numerical studies, e.g., Rechenmacher [45] and Guo [24], have shown that the shear band thickness is governed by the critical particle-column length aligned in the direction of shear and compression. Here, this concept is adopted to interpret the observed increase in shear band thickness with fines content. Fig. 21 (c)-(d) illustrates the meso- and micro-scale mechanisms. In clean, coarse-grained soils without fines, shear bands form through the buckling of aligned columns of coarse particles. The critical length of these columns determines the shear band thickness, which is primarily a function of particle size and arrangement. When fines are introduced (Fig. 21 (e)), they fill the voids between coarse particles and begin to participate in load transfer during shearing. These fine particles interact with neighbouring grains via sliding and rotation, effectively becoming part of the load-bearing force chains. A force chain may be approximated as a three-particle segment, and the critical buckling threshold of such a segment can be estimated using an Euler-like expression:

$$F_{cr} = \frac{\alpha k_n R^3}{L^2} \tag{8}$$

where F_{cr} represents critical normal contact force required to trigger buckling of the force chain segment, k_n is the normal contact stiffness between particles, R is the particle radius, L is the critical particle-column length and α is a coefficient dependent on boundary conditions and particle geometry, typically determined through DEM calibration. The presence of fines reduces the effective normal contact force within force chain [57], which, according to the above relation, increases the critical column length required for buckling. Additionally, fines increase the number of particles per column, extending the length and complexity of the force chains. As a result, the effective thickness of the shear band increases due to the broader spatial extent of strain localization, as shown in Fig. 21 (e). These results, obtained both from Triaxial-DVC and Triaxial-DIC, corroborate the three-stage deformation process from both experimental and microstructural perspectives, transitioning from homogeneous strain to localized deformation and finally to a persistent shear band.

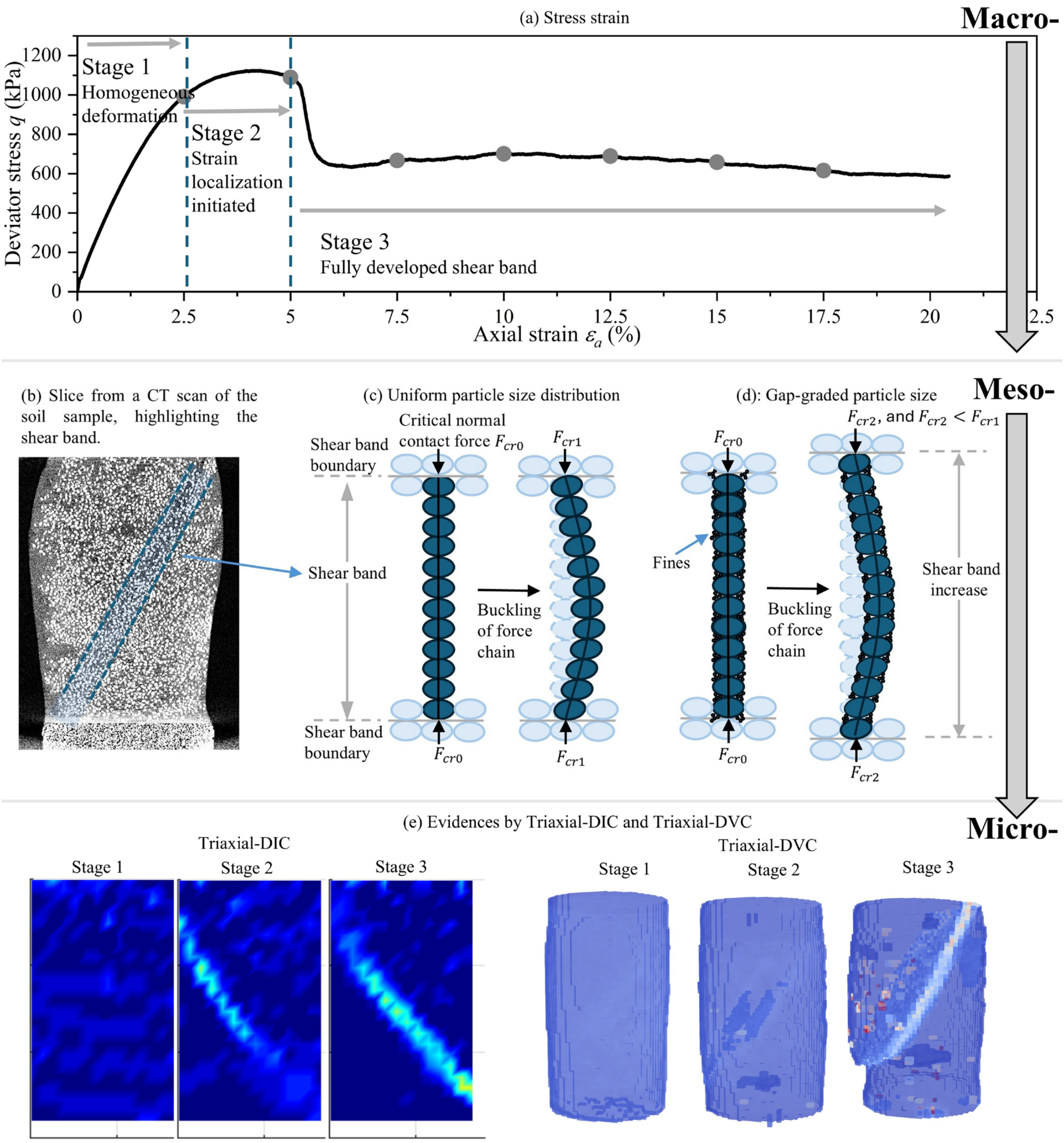

Fig. 21. (a) macroscopic stress-strain behaviour; (b-d) schematic interpretation of mesoscopic mechanism within a fully developed shear band under shearing; (e) strain field obtained from Triaxial-DIC and -DVC.

6. Conclusion

This study examined the influence of fines content on shear band formation and thickness in sands, and compared the capabilities of Triaxial-DIC and Triaxial-DVC for shear band characterisation. A series of triaxial shearing tests was performed on gap-graded sand samples with varying fines content, with shear band development and residual thickness quantified from surface strain fields using DIC and from internal deformation fields using DVC. The main conclusions are:

- Residual shear band thicknesses measured by DIC and DVC were nearly identical. For example, at 20% fines content, DIC and DVC gave mean values of 3.408 mm and 3.420 mm, respectively, with comparable variance, confirming that DIC can reliably quantify thickness when volumetric measurements are not feasible.
- Increasing fines content systematically broadened the normalised residual shear band thickness (thickness / mean particle size), which increased linearly from ~7.62 to ~11.66 as fines content rose from 0% to 40%. This relationship was consistently captured by both DIC and DVC, indicating fines as a primary control on strain localisation extent.
- DVC revealed early, spatially non-uniform strain localisation and secondary shear plane formation prior to peak strength, features not detected by DIC, highlighting its capacity for microstructural and 3D deformation analysis.
- DIC offers efficient, fast, and low-cost surface measurements, while DVC provides detailed volumetric characterisation. Their combined use yields both efficiency and completeness in experimental programmes.
- An example interpretation is presented to mechanistically explain why increasing fines content in sands promotes shear band thickening, integrating macro-, meso-, and micro-scale observations.

CRediT authorship contribution statement

Shijin Li: Conceptualization, Methodology, Software, Investigation, Formal analysis, Data curation, Writing-original draft, Visualization. **Alexandre Sac-Morane**: Software, Writing-review & editing. **Jeroen Soete**: Supervision, Project administration, Writing-review & editing. **Hannes Claes:** Resources, Writing-review & editing. **Johan Vanhulst**: Resources, Project administration; **Hadrien Rattez**: Conceptualization, Methodology, Writing-review & editing, Supervision, Project administration, Funding acquisition.

Acknowledgments and funding

The authors gratefully acknowledge the financial support of the Belgium Energy Transition Fund (ETF) through the SAGE-SAND project (Soil Aging Around Offshore Wind Turbine Foundations - From Operational Response to Decommissioning, grant number 3E220974) and the National Natural Science Foundation of China (52308370). The KU Leuven XCT Core Facility is acknowledged for the 3D image acquisition and processing tools (https://xct.kuleuven.be/). The authors also thank Professor Edward Andò and his colleagues Dr. Gustavo Pinzón, Dr. Olga Stamati, and Dr. Max Wiebicke for their technical guidance and training on digital volume correlation using SPAM software.

Software and data availability statement

The software for Triaxial-DIC was developed by the authors and released as open-source, making it available at AlexSacMorane/DIC: Digital Image Correlation (github.com). Additionally, the open-source software for DVC, SPAM: Software for Practical Analysis of Materials (Stamati et al., 2020), is also available online. All experimental data supporting the findings of this study are available from the first author upon reasonable request.

Conflict of interest

The authors declare that they have no conflict of interest.

REFERECES

[1] Abdullah-Al-Wadud M, Kabir Md, Akber Dewan M, Chae O (2007) A dynamic histogram equalization for image contrast enhancement. IEEE Trans Consumer Electron 53:593–600. https://doi.org/10.1109/TCE.2007.381734

[2] Adesina P, Wautier A, Benahmed N (2025) The mechanical behaviour of gap-graded soils under triaxial compression and extension loading paths. Acta Geotech. https://doi.org/10.1007/s11440-025-02600-3

[3] Alonso-Marroquin F, Vardoulakis I (2005) Micromechanics of shear bands in granular media. In: Proceedings of the International Conference on Powders & Grains 2005. CRC Press, Stuttgart, Germany, pp 701–704

[4] Alshibli KA, Hasan A (2008) Spatial variation of void ratio and shear band thickness in sand using X-ray computed tomography. Géotechnique 58:249–257. https://doi.org/10.1680/geot.2008.58.4.249

[5] Alshibli KA, Sture S (1999) Sand shear band thickness measurements by digital imaging techniques. J Comput Civ Eng 13:103–109. https://doi.org/10.1061/(asce)0887-3801(1999)13:2(103)

[6] Andò E, Hall SA, Viggiani G, et al (2012) Grain-scale experimental investigation of localised deformation in sand: a discrete particle tracking approach. Acta Geotech 7:1–13. https://doi.org/10.1007/s11440-011-0151-6

[7] Andò E, Viggiani G, Hall SA, Desrues J (2013) Experimental micro-mechanics of granular media studied by x-ray tomography: recent results and challenges. Geotech Lett 3:142–146. https://doi.org/10.1680/geolett.13.00036

[8] ASTM D4253 (2019) Standard test methods for maximum index density and unit weight of soils using a vibratory table

[9] ASTM D4254 (2016) Standard test methods for minimum index density and unit weight of soils and calculation of relative density

[10] ASTM D7181-20 (2020) Standard test method for consolidated drained triaxial compression test for soils. ASTM D7181-20

[11] Bésuelle P, Chambon R, Collin F (2006) Switching deformation modes in post-localization solutions with a quasibrittle material. J Mech Mater Struct 1:1115–1134. https://doi.org/10.2140/jomms.2006.1.1115

[12] Bhandari AR, Powrie W, Harkness RM (2012) A digital image-based deformation measurement system for triaxial tests. Geotech Test J 35:209–226.

https://doi.org/10.1520/GTJ103821

[13] Borja RI, Lai TY (2002) Propagation of localization instability under active and passive loading. J Geotech Geoenviron Eng 128:64–75. https://doi.org/10.1061/(ASCE)1090-0241(2002)128:1(64)

[14] Carraro JAH, Prezzi M, Salgado R (2009) Shear strength and stiffness of sands containing plastic or nonplastic fines. J Geotech Geoenviron Eng 135:1167–1178. https://doi.org/10.1061/(ASCE)1090-0241(2009)135:9(1167)

[15] Chang CS, Yin Z-Y (2011) Micromechanical modeling for behavior of silty sand with influence of fine content. Int J Solids Struct 48:2655–2667. https://doi.org/10.1016/j.ijsolstr.2011.05.014

[16] Chen Z, Shao X, Xu X, He X (2018) Optimized digital speckle patterns for digital image correlation by consideration of both accuracy and efficiency. Appl Opt 57:884. https://doi.org/10.1364/AO.57.000884

[17] Chu J, Lo SCR, Lee IK (1996) Strain softening and shear band formation of sand in multi-axial testing. Géotechnique 46:63–82. https://doi.org/10.1680/geot.1996.46.1.63

[18] Desrues J, Andò E, Mevoli FA, et al (2018) How does strain localise in standard triaxial tests on sand: Revisiting the mechanism 20 years on. Mech Res Commun 92:142–146. https://doi.org/10.1016/j.mechrescom.2018.08.007

[19] Desrues J, Viggiani G (2004) Strain localization in sand: an overview of the experimental results obtained in Grenoble using stereophotogrammetry. Int J Numer Anal Methods Geomech 28:279–321. https://doi.org/10.1002/nag.338

[20] Dong YL, Pan B (2017) A review of speckle pattern fabrication and assessment for digital image correlation. Exp Mech 57:1161–1181. https://doi.org/10.1007/s11340-017-0283-1

[21] Fu P, Dafalias YF (2011) Fabric evolution within shear bands of granular materials and its relation to critical state theory. Int J Numer Anal Methods Geomech 35:1918–1948. https://doi.org/10.1002/nag.988

[22] Gao Z, Zhao J (2013) Strain localization and fabric evolution in sand. Int J Solids Struct 50:3634–3648. https://doi.org/10.1016/j.ijsolstr.2013.07.005

[23] Gudehus G, Nübel K (2004) Evolution of shear bands in sand. Géotechnique 54:187–201. https://doi.org/10.1680/geot.2004.54.3.187

[24] Guo P (2012) Critical length of force chains and shear band thickness in dense granular materials. Acta Geotech 7:41–55. https://doi.org/10.1007/s11440-011-0154-3

[25] Hall SA, Bornert M, Desrues J, et al (2010) Discrete and continuum analysis of

localised deformation in sand using X-ray µCT and volumetric digital image correlation. Géotechnique 60:315–322. https://doi.org/10.1680/geot.2010.60.5.315

[26] Han C, Drescher A (1993) Shear bands in biaxial tests on dry coarse sand. Soils and Foundations 33:118–132. https://doi.org/10.3208/sandf1972.33.118

[27] Haralock RM, Shapiro LG (1992) Computer and robot vision. Addison-Wesley Longman Publishing Co., Inc, Boston, Massachusetts, USA

[28] Heap MJ, Baud P, McBeck JA, et al (2020) Imaging strain localisation in porous andesite using digital volume correlation. J Volcanol Geotherm Res 404:107038. https://doi.org/10.1016/j.jvolgeores.2020.107038

[29] Kak AC, Slaney M (2001) Principles of Computerized Tomographic Imaging. Society for Industrial and Applied Mathematics

[30] Kikumoto M, Muir Wood D, Russell A (2010) Particle crushing and deformation behaviour. Soils Found 50:547–563. https://doi.org/10.3208/sandf.50.547

[31] Ladd RS (1978) Preparing test specimens using undercompaction. Geotech Test J 1:16. https://doi.org/10.1520/GTJ10364J

[32] Lewis JP (1995) Fast template matching. In: Vision interface. Quebec City, QC, Canada, pp 15–19

[33] Li S, Russell AR, Muir Wood D (2024) Internal erosion of gap-graded soil and influences on the critical state. Acta Geotech 19:5363–5381. https://doi.org/10.1007/s11440-024-02249-4

[34] Li Y, Otsubo M, Ghaemi A, et al (2022) Transition of gap-graded soil fabric-shear wave measurements and dispersion relation. Soils Found 62:101092. https://doi.org/10.1016/j.sandf.2021.101092

[35] Mühlhaus HB, Vardoulakis I (1987) The thickness of shear bands in granular materials. Géotechnique 37:271–283. https://doi.org/10.1680/geot.1987.37.3.271

[36] Muir Wood D, Maeda K (2008) Changing grading of soil: effect on critical states. Acta Geotech 3:3–14. https://doi.org/10.1007/s11440-007-0041-0

[37] Nguyen CD, Benahmed N, Andò E, et al (2019) Experimental investigation of microstructural changes in soils eroded by suffusion using X-ray tomography. Acta Geotech 14:749–765. https://doi.org/10.1007/s11440-019-00787-w

[38] Oda M, Kazama H (1998) Microstructure of shear bands and its relation to the mechanisms of dilatancy and failure of dense granular soils. Géotechnique 48:465–481. https://doi.org/10.1680/geot.1998.48.4.465

[39] Pinzón G (2020) Experimental investigation of the effects of particle shape and friction

on the mechanics of granular media. Dissertation, Université Grenoble Alpes

[40] Pinzón G, Andò E, Desrues J, Viggiani G (2023) Fabric evolution and strain localisation in inherently anisotropic specimens of anisometric particles (lentils) under triaxial compression. Granul Matter 25:15. https://doi.org/10.1007/s10035-022-01305-8

[41] Rattez H, Shi Y, Sac-Morane A, et al (2022) Effect of grain size distribution on the shear band thickness evolution in sand. Géotechnique 72:350–363. https://doi.org/10.1680/jgeot.20.P.120

[42] Rattez H, Stefanou I, Sulem J, et al (2018) Numerical analysis of strain localization in rocks with thermo-hydro-mechanical couplings using cosserat continuum. Rock Mech Rock Eng 51:3295–3311. https://doi.org/10.1007/s00603-018-1529-7

[43] Rattez H, Veveakis M (2020) Weak phases production and heat generation control fault friction during seismic slip. Nat Commun 11:1–8. https://doi.org/10.1038/s41467-019-14252-5

[44] Rechenmacher A, Finno R (2004) Digital image correlation to evaluate shear banding in dilative sands. Geotech Test J 27:13–22. https://doi.org/10.1520/GTJ11263J

[45] Rechenmacher AL (2006) Grain-scale processes governing shear band initiation and evolution in sands. J Mech Phys Solids 54:22–45. https://doi.org/10.1016/j.jmps.2005.08.009

[46] Rechenmacher AL, Abedi S, Chupin O, Orlando AD (2011) Characterization of mesoscale instabilities in localized granular shear using digital image correlation. Acta Geotech 6:205–217. https://doi.org/10.1007/s11440-011-0147-2

[47] Reu PL, Sweatt W, Miller T, Fleming D (2015) Camera system resolution and its influence on digital image correlation. Exp Mech 55:9–25. https://doi.org/10.1007/s11340-014-9886-y

[48] Salgado R, Bandini P, Karim A (2000) Shear strength and stiffness of silty sand. J Geotech Geoenviron Eng 126:451–462. https://doi.org/10.1061/(ASCE)1090-0241(2000)126:5(451)

[49] Schneider CA, Rasband WS, Eliceiri KW (2012) NIH Image to ImageJ: 25 years of image analysis. Nat Methods 9:671–675. https://doi.org/10.1038/nmeth.2089

[50] Seguí C, Rattez H, Veveakis M (2020) On the stability of deep-seated landslides. The cases of Vaiont (Italy) and shuping (Three Gorges Dam, China). J Geophys Res Earth Surf 125:e2019JF005203. https://doi.org/10.1029/2019JF005203

[51] Shahin G, Hurley RC (2022) Micromechanics and strain localization in sand in the ductile regime. J Geophys Res: Solid Earth 127:1–19. https://doi.org/10.1029/2022JB024983

[52] Shi XS, Liu K, Yin J (2021) Effect of initial density, particle shape, and confining stress on the critical state behavior of weathered gap-graded granular soils. J Geotech Geoenviron Eng 147:04020160. https://doi.org/10.1061/(ASCE)GT.1943-5606.0002449

[53] Shire T, O'Sullivan C, Hanley KJ, Fannin RJ (2014) Fabric and effective stress distribution in internally unstable soils. J Geotech Geoenviron Eng 140:04014072. https://doi.org/10.1061/(ASCE)GT.1943-5606.0001184

[54] Smith SAF, Nielsen S, Toro GD (2015) Strain localization and the onset of dynamic weakening in calcite fault gouge. Earth Planet Sci Lett 413:25–36. https://doi.org/10.1016/j.epsl.2014.12.043

[55] Soltanbeigi B, Altunbas A, Cinicioglu O (2021) Influence of dilatancy on shear band characteristics of granular backfills. Eur J Environ Civ Eng 25:1201–1218. https://doi.org/10.1080/19648189.2019.1572542

[56] Stamati O, Andò E, Roubin E, et al (2020) Spam: software for practical analysis of materials. Int J Open Source Softw Process 5:2286. https://doi.org/10.21105/joss.02286

[57] Sufian A, Artigaut M, Shire T, O'Sullivan C (2021) Influence of fabric on stress distribution in gap-graded soil. J Geotech Geoenviron Eng 147:04021016. https://doi.org/10.1061/(ASCE)GT.1943-5606.0002487

[58] Thevanayagam S, Shenthan T, Mohan S, Liang J (2002) Undrained fragility of clean sands, silty sands, and sandy silts. J Geotech Geoenviron Eng 128:849–859. https://doi.org/10.1061/(ASCE)1090-0241(2002)128:10(849)

[59] Tordesillas A (2007) Force chain buckling, unjamming transitions and shear banding in dense granular assemblies. Phil Mag 87:4987–5016. https://doi.org/10.1080/14786430701594848

[60] Tordesillas A, Muthuswamy M, Walsh SD (2008) Mesoscale measures of nonaffine deformation in dense granular assemblies. J Eng Mech 134:1095–1113. https://doi.org/10.1061/(ASCE)0733-9399(2008)134:12(1095)

[61] Vallejo LE (2001) Interpretation of the limits in shear strength in binary granular mixtures. Can Geotech J 38:1097–1104. https://doi.org/10.1139/t01-029

[62] Vardoulakis I, Aifantis EC (1991) A gradient flow theory of plasticity for granular materials. Acta Mech 87:197–217. https://doi.org/10.1007/BF01299795

[63] Vardoulakis I, Graf B (1985) Calibration of constitutive models for granular materials using data from biaxial experiments. Géotechnique 35:299–317. https://doi.org/10.1680/geot.1985.35.3.299

[64] Vardoulakis IG, Sulem J (1995) Bifurcation analysis in geomechanics. Chapman & Hall, Glasgow, UK

[65] Wiebicke M, Andò E, Viggiani G, Herle I (2020) Measuring the evolution of contact fabric in shear bands with X-ray tomography. Acta Geotech 15:79–93. https://doi.org/10.1007/s11440-019-00869-9

[66] Wiebicke M, Herle I, Andò E, Viggiani G (2021) Measuring the fabric evolution of sand - application and challenges. Geotechnik 44:114–122. https://doi.org/10.1002/gete.202000019

[67] Xiao Y, Xiang J, Liu H, Ma Q (2017) Strength-dilatancy relation of sand containing non-plastic fines. Geotech Lett 7:204–210. https://doi.org/10.1680/jgele.16.00144

[68] Yilmaz Y, Deng Y, Chang CS, Gokce A (2023) Strength-dilatancy and critical state behaviours of binary mixtures of graded sands influenced by particle size ratio and fines content. Géotechnique 73:202–217. https://doi.org/10.1680/jgeot.20.P.320

[69] Yin Z-Y, Huang H-W, Hicher P-Y (2016) Elastoplastic modeling of sand–silt mixtures. Soil Found 56:520–532. https://doi.org/10.1016/j.sandf.2016.04.017

[70] Yin Z-Y, Zhao J, Hicher P-Y (2014) A micromechanics-based model for sand-silt mixtures. Int J Solids Struct 51:1350–1363. https://doi.org/10.1016/j.ijsolstr.2013.12.027

[71] Zhu Y, Nie Z, Gong J, et al (2020) An analysis of the effects of the size ratio and fines content on the shear behaviors of binary mixtures using DEM. Comput Geotech 118:103353. https://doi.org/10.1016/j.compgeo.2019.103353